https://doi.org/10.5194/egusphere-2026-659
Preprint. Discussion started: 5 February 2026

Characteristics of tropical clouds with strong updrafts revealed by Doppler velocity measurements from EarthCARE/CPR

Haruka Hotta[1,2], Kentaroh Suzuki[1], Maki Kikuchi[2], Shunsuke Aoki[2], Takuji Kubota[2]

[1]Atmosphere and Ocean Research Institute, University of Tokyo, Kashiwa, 277-8564, Japan
[2]Earth Observation Research Center, Japan Aerospace Exploration Agency, Tsukuba, 305-8505, Japan

Correspondence to: Haruka Hotta (hotta@aori.u-tokyo.ac.jp)

Abstract. Updrafts within clouds are important for the climate system, yet global assessments have traditionally relied on indirect proxies. The EarthCARE satellite's 94 GHz Cloud Profiling Radar (CPR) provides the first global, spaceborne Doppler velocity (Vd) profiles of clouds, enabling direct constraints on convective updraft intensity beyond proxy-based diagnostics. We analyze CPR cloud-property products over the tropics and extract convectively driven columns. We define *MaxVd* as the maximum upward Vd within the subfreezing portion of each column. Columns with *MaxVd* > 2.5 m s^{-1} are classified as strong-updraft (SU) columns. They exhibit systematically higher echo-top heights at 0 and 10 dBZ than weaker-updraft columns, linking microphysics to dynamics. The probability of SU occurrence strongly depends on the separation between the cloud top and the 0 dBZ echo top, defined as ΔH. A small ΔH robustly identifies SU, including relatively low-topped systems. Spatiotemporally, SU occurrence is enhanced over land, with notably higher values at the 14:00 local-time overpass than at 02:00. In contrast, oceanic regions have a smaller SU fraction and exhibit a weaker difference between the two overpass times. These SU enhancements primarily reflect a shift toward horizontally compact, small-ΔH systems rather than higher cloud tops alone. Doppler folding preferentially occurs in small-ΔH structures, with maxima during the continental afternoon, providing a qualitative tracer of extreme updrafts. The combined constraints from Doppler-derived updraft intensity and echo structure offer a process-oriented benchmark for evaluating the coupling between convective dynamics and microphysics in numerical models.

1 Introduction

Updrafts within tropical deep clouds promote the activation and condensational growth of cloud droplets and the formation of precipitation particles, thereby exerting strong control over the timing, amount, and intensity of rainfall. The strength of these updrafts also determines the maximum height reached by convective clouds and the horizontal extent of their anvils. Within the Earth's climate system, convective updrafts therefore constitute a key dynamical element. Through the rapid ascent of moist air and the associated release of latent heat, they drive large-scale overturning circulations such as the Hadley and Walker cells

https://doi.org/10.5194/egusphere-2026-659
Preprint. Discussion started: 5 February 2026

and contribute to meridional energy transport from the tropics to the midlatitudes (Manabe et al., 1965; Tiedtke, 1989; Bechtold et al., 2001). Vigorous updrafts shape the spatial distribution of rainfall and the occurrence of extreme precipitation events. In addition, the heights and lifetimes of deep clouds, which are controlled by updrafts, exert a strong influence on the planetary energy budget by reflecting incoming shortwave radiation and trapping outgoing longwave radiation (Ramanathan et al., 1989; Hartmann et al., 2001). Updrafts are also crucial in the context of global warming projections: the representation of convective mixing and mass flux in global models affects simulated climate sensitivity and helps explain the spread in equilibrium climate sensitivity across models (Zhao, 2014; Sherwood et al., 2014).

Despite this central role, direct observations of updraft vertical velocity (w) in tropical deep clouds remain sparse, limiting our ability to evaluate and improve its representation in atmospheric models. Surface-based and airborne radars have provided invaluable snapshots of w (Heymsfield et al., 2010; Collis et al., 2013; Giangrande et al., 2016; Schiro et al., 2018; Schumacher et al., 2015), but these measurements are episodic, geographically restricted, and heavily concentrated over land. Consequently, global model evaluation still relies primarily on bulk fields and rainfall statistics rather than on the convective processes themselves (Maloney et al., 2019). General circulation models that employ cumulus parameterizations exhibit several persistent, systematic biases, including the double-ITCZ bias and excessively early diurnal peaks in precipitation amount and frequency. These deficiencies point to structural shortcomings in current parameterizations and motivate a fundamental reassessment (Christopoulos and Schneider, 2021; Tian and Dong, 2020). Even at cloud-resolving scales, state-of-the-art numerical models struggle to reproduce the observed statistics and vertical structure of w and its interaction with cloud microphysics. Recent intercomparisons of global km-scale models reveal substantial spread in the magnitude of updrafts: the fraction of columns in which the maximum vertical velocity exceeds 10–20 m s^{-1} can differ by more than an order of magnitude across models, and simulated regional patterns of convective strength vary widely (Abbott et al., 2025). Takahashi et al. (2025) similarly demonstrated that global km-scale simulations fail to adequately represent the regional variability of convective intensity and exhibit an unrealistic relationship between updrafts and precipitation formation processes. Together, these discrepancies underscore a critical need for global, observation-based constraints on w to calibrate both parameterized convection in general circulation models (GCMs) and explicitly simulated convection in global km-scale models.

Spaceborne measurements have helped address the lack of comprehensive observations of w for model evaluation by providing systematic, globally distributed samples of deep cloud systems. However, because most satellite instruments cannot directly observe vertical motion, satellite-based studies have relied on proxy diagnostics for convective intensity. For instance, infrared imagers use 11–12 μm brightness temperatures to track overshooting tops and to document the diurnal cycle of cloud-top extent (Bedka et al., 2010; Yang and Slingo, 2001). Attempts have been made to infer cloud-top vertical velocities from the temporal evolution of cloud-top temperature; however, methodological uncertainties and a focus on developing clouds have so far prevented these approaches from yielding a comprehensive, global-scale picture across cloud regimes (Adler and Fenn, 1979; Luo et al., 2014; Hamada and Takayabu, 2016). Passive microwave radiometers exploit scattering and absorption at approximately 89 and 166–183 GHz to infer convective intensity (Mohr and Zipser, 1996; Skofronick-Jackson et al., 2017). Other studies use lightning flash rates—which are closely linked to the collision rates of ice particles in strong updrafts—as

https://doi.org/10.5194/egusphere-2026-659
Preprint. Discussion started: 5 February 2026

indicators of the most vigorous convection (Christian et al., 2003; Williams and Stanfill, 2002; Deierling and Petersen, 2008; Cecil et al., 2005). The Tropical Rainfall Measuring Mission (TRMM; 1997–2015) and its successor, the Global Precipitation Measurement (GPM; 2014–present) mission, have provided unprecedented global views of precipitation using spaceborne precipitation radars (Kummerow et al., 1998; Iguchi et al., 2000; Hou et al., 2014; Skofronick-Jackson et al., 2017). From these observations, researchers have developed widely used proxies for convective intensity. One common proxy is the echo-top height (ETH), defined as the highest altitude at which a specified reflectivity threshold (e.g., 20, 30, or 40 dBZ) is detected. ETH is interpreted as the altitude reached by large, precipitating hydrometeors (Zipser et al., 2006; Liu and Zipser, 2005; Romatschke et al., 2010). Collectively, these proxy-based studies have revealed robust climatological features, including enhanced convective intensity over land compared with the ocean (Williams et al., 2005; Liu and Zipser, 2008; Zipser et al., 2006).

The A-Train constellation further advanced vertical profiling through CloudSat's 94 GHz Cloud Profiling Radar (CPR), which is sensitive to clouds and light-to-moderate precipitation and resolves the vertical structure of clouds with horizontal and vertical resolutions of approximately 1 km and 240 m, respectively (Stephens et al., 2002; Tanelli et al., 2008; Stephens et al., 2008). Compared with the TRMM (13.8 GHz) and GPM (13.6 and 35.55 GHz) precipitation radars, CPR has higher sensitivity, detecting clouds with reflectivity as low as about −28 dBZ (Stephens et al., 2008), and its smaller horizontal footprint provides more detailed information on convective cloud structure. Several proxy metrics for convective intensity based on CPR profiles have been proposed. One class of metrics uses cloud-top height (CTH) and echo-top height (ETH) at thresholds of 0 or 10 dBZ. Stronger updrafts are expected to loft larger hydrometeors to higher levels and therefore result in greater ETH (Luo et al., 2011; Takahashi and Luo, 2014). Another class uses the separation between CTH and ETH at 0 or 10 dBZ: when both small and large particles are carried to similarly high levels, CTH and ETH converge (Luo et al., 2008; Luo et al., 2011; Takahashi and Luo, 2014). Regional composites of these proxies reaffirm geographic variations in convective intensity and relate them to environmental controls. For example, Takahashi et al. (2023) demonstrated a strong land–ocean contrast, with hotspots over equatorial Africa and the Amazon, whereas convection over the Maritime Continent is comparatively weaker. Another diagnostic, the cloud center of gravity (COG), defined as the reflectivity-weighted mean height of the cloud within a column, has also been used to characterize convective structure (Koren et al., 2009). COG is especially high over the tropical West African Basin and the Congo Basin (Pilewskie and L'Ecuyer, 2022).

Although many previous studies have sought to characterize convective updraft intensity at the global scale, two major limitations remain. First, a fundamental shortcoming of these approaches is that they do not directly measure vertical motion. Proxy indicators do not have a simple or universal correspondence with w, and their relationships vary across different dynamical regimes (Takahashi and Luo, 2014; Liu et al., 2007). Consequently, even with extensive satellite archives, direct, observation-based constraints on w at the global scale have remained out of reach. Second, most proxy-based climatologies are designed to preferentially sample specific types of clouds. The precipitation radars aboard TRMM and GPM primarily detect fully developed, tall convective systems with strong radar echoes because, owing to their relatively low sensitivity, they must rely on high reflectivity thresholds (20–30 dBZ). These thresholds are intrinsically insensitive to weaker hydrometeor

https://doi.org/10.5194/egusphere-2026-659
Preprint. Discussion started: 5 February 2026

populations. Lightning-based metrics emphasize only the most strongly electrified convective cores, while infrared-based ascent-rate approaches focus exclusively on rapidly developing cloud tops. Even studies using CloudSat, which is capable of detecting weak echoes, have often concentrated on tall, well-developed clouds, partly because only a limited set of observable parameters—essentially radar reflectivity—can be robustly analyzed. Consequently, the resulting "intensity" maps that have guided our understanding of convection primarily reflect the upper tail of convective vigor and under-represent relatively low-topped or weak-echo clouds, as well as life-cycle stages outside peak development (Takahashi and Luo, 2014; Hamada et al., 2015; Xu et al., 2022).

A decisive advance has become possible with the Earth Cloud, Aerosol and Radiation Explorer (EarthCARE), a joint mission of ESA and JAXA launched in May 2024. EarthCARE carries a 94-GHz Doppler Cloud Profiling Radar (CPR), together with a high-spectral-resolution lidar, a multispectral imager, and broadband radiometers (Illingworth et al., 2015; Wehr et al., 2023). Crucially, the EarthCARE CPR provides nadir profiles of both radar reflectivity and Doppler velocity, enabling the first direct measurements of vertical motions within clouds at the global scale. The high sensitivity of EarthCARE's 94-GHz radar allows the detection of weak reflectivity, thereby systematically sampling shallow, weak-echo convective clouds as well as deep convective systems. EarthCARE is therefore well suited for evaluating vertical motions across a broad range of convective clouds (Illingworth et al., 2015).

Building on this novel capability, this study presents the first global characterization of convective updrafts based on Doppler velocity measurements from the EarthCARE CPR. The primary objectives are threefold: (1) to develop a method for identifying updraft strength in tropical deep convective clouds using quality-controlled Doppler velocities; (2) to investigate how updraft strength relates to the vertical structure of radar reflectivity, thereby probing links between cloud dynamics and microphysical processes and comparing these relationships with those inferred from legacy satellite proxies; and (3) to map the global distribution of updraft intensity and examine its dependence on variations in cloud morphological properties. Sect. 2 describes the EarthCARE CPR data and analysis methodology used in this study, Sect. 3 presents the results, and Sect. 4 summarizes the findings and discusses their implications.

2 Data and analysis method

2.1 Datasets

We use measurements from the Cloud Profiling Radar (CPR) aboard the EarthCARE satellite. EarthCARE flies in a sun-synchronous, near-polar orbit (inclination 97.05°) with nominal local equator-crossing times near 02:00 local time (ascending) and 14:00 local time (descending) (Wehr et al., 2023). The 94-GHz CPR provides nadir profiles of radar reflectivity and Doppler radial velocity. Its intrinsic vertical resolution is 500 m, while the profiles are sampled every 100 m in the vertical. The instantaneous, beam-limited horizontal footprint is approximately 750 m at nadir, with profiles sampled at about 500 m intervals along track.

https://doi.org/10.5194/egusphere-2026-659
Preprint. Discussion started: 5 February 2026

The variables used in this analysis are taken from the standard CPR one-sensor cloud property product (CPR_CLP, version Bb; JAXA, 2025a), specifically the cloud mask, radar reflectivity factor (Ref), Doppler velocity (Vd), and air temperature. These data have a horizontal resolution of 1 km and a vertical sampling of 100 m. In CPR_CLP, the Level-1B received echo power and Doppler velocities are remapped onto the same grid as the cloud mask. Second-trip echoes (mirror images) are screened following Battaglia (2021), as implemented by Aoki et al. (2026). The cloud mask is derived using noise screening, echo-continuity tests, and surface-echo diagnostics (Sato et al., 2025). Air temperature is provided by a JAXA auxiliary product that interpolates temperatures from ECMWF forecasts (Eisinger et al., 2024) to the EarthCARE Level-2 grid (JAXA, 2025b). In this study, positive (negative) Vd denotes upward (downward) motion.

2.2 Column selection criteria

We exploit EarthCARE's Doppler capability to analyze vertical velocity *w* even in clouds with weak radar echoes. We focus on the tropical region (30° S–30° N) for the period January–September 2025. Data collected prior to early December 2024 are discarded to avoid known noise in Doppler velocity within weaker echoes associated with operation of a redundant side of the signal processing unit in the CPR instrument (JAXA, 2025c), thereby ensuring data quality. Because Doppler-based diagnostics are restricted to range gates with temperatures below 273.15 K (as discussed in Sect. 2.3), we retain only columns that contain a substantial cold portion. To focus on convectively driven clouds, we extract columns that satisfy all of the following conditions:

(1) Single-layer cloud. Using the cloud mask, a gate is regarded as "cloudy" when the cloud-mask value is ≥ 20 (weak echo). All gates between the highest and lowest cloudy gates must be classified as cloudy.

(2) Thermodynamic bounds. The cloud-top temperature (CTT) is < 258.15 K, and the cloud-base temperature is > 273.15 K.

(3) Geometrical thickness. The difference between cloud-top height and cloud-base height exceeds 5 km.

(4) Reflectivity strength. The column-maximum Ref exceeds 0 dBZ.

2.3 Doppler-velocity quality control

CPR Doppler velocities are affected by several sources of error: random noise arising from reduced correlation between successive pulses caused by the rapid motion of the satellite platform (ε_random; Doviak and Zrnic, 2014; Hagihara et al., 2023); pointing uncertainty due to satellite attitude perturbations and antenna thermal distortion (ε_pointing; Tanelli et al., 2005); multiple scattering (ε_MS; Battaglia et al., 2011); non-uniform beam-filling effects (ε_NUBF); and velocity aliasing beyond the Nyquist limit (ε_Nyquist; Sy et al., 2014).

To correct for ε_pointing, we apply a bias correction based on the assumption that the Doppler velocity averaged horizontally over 100 km at the surface is zero (Aoki et al., 2026). To limit ε_NUBF, which is large near cloud boundaries and in weak-reflectivity regions, we retain only gates that simultaneously satisfy a cloud-mask value ≥ 20 and Ref ≥ −19 dBZ. To mitigate

https://doi.org/10.5194/egusphere-2026-659
Preprint. Discussion started: 5 February 2026

ε_MS, we follow Battaglia et al. (2011) and exclude range bins for which the cumulative reflectivity from the top of the atmosphere down to that gate exceeds a prescribed threshold. The CPR Nyquist (folding) velocity is approximately ±5–6 m s^{-1}; therefore, large downward (negative) velocities associated with the sedimentation of large particles can be aliased, especially at temperatures above 273.15 K, despite the first-pass dealiasing applied following Hagihara et al. (2023). For this reason, all Doppler-based diagnostics are restricted to subfreezing gates (i.e., temperatures below 273.15 K).

2.4 Metric for updraft strength

We identify columns affected by residual folding (aliasing) at temperatures below 273.15 K as follows. First, for gates colder than 273.15 K, we compute along-track means of Vd over 3 km windows to reduce random error and small-scale turbulent variability. If any pixel within a 3 km window fails the quality filters (cloud-mask value < 20 or Ref < −19 dBZ), that window is excluded from the analysis. We then examine vertical differences in the 3 km–averaged Vd profiles and flag as folded those columns in which the jump in Vd between adjacent vertical gates exceeds the Nyquist velocity. The folded columns are used to characterize the strength of convective updrafts, rather than being completely excluded from the analysis.

For columns that are not flagged as folded, we define a Vd-based updraft metric to quantitatively characterize the convective intensity of each column. For all remaining gates colder than 273.15 K, Vd is averaged over 3-km along-track windows and then over two adjacent vertical gates (200 m) to reduce random errors and small-scale variability. If any pixel within an averaging window fails the validity filters (cloud-mask value < 20 or reflectivity < −19 dBZ), that window is discarded. This procedure effectively removes cloud-edge regions. We then define *MaxVd*, the column-maximum Doppler velocity, as the largest Vd within the portion of the 3-km– and 200-m–averaged profile that is colder than 273.15 K for columns that are not flagged as folded. As a result, columns associated with extremely strong updrafts, for which folding is more likely to occur (Galfione et al., 2025), may be excluded from the *MaxVd*-based analysis.

Using an extreme-value metric such as the column-maximum Doppler velocity (*MaxVd*) preferentially captures embedded updraft cores that dominate momentum and mass transport. In contrast, the mean or median Vd is more sensitive to measurement noise. Similar “maximum” or high-percentile Doppler metrics have been used as proxies for convective intensity and for evaluating model clouds (Heymsfield et al., 2010; Abbott et al., 2025). The 3-km along-track and two-gate (200 m) vertical averaging scales are tunable choices; however, the main results are insensitive to reasonable variations in these parameters. We also tested an alternative column metric, namely the volume fraction of gates for which Vd exceeds a fixed threshold. The qualitative conclusions are unchanged when this alternative metric is used instead of *MaxVd*, indicating that our findings are robust to the specific choice of updraft indicator.

2.5 Case examination of V_d quality control and the updraft metric

https://doi.org/10.5194/egusphere-2026-659
Preprint. Discussion started: 5 February 2026

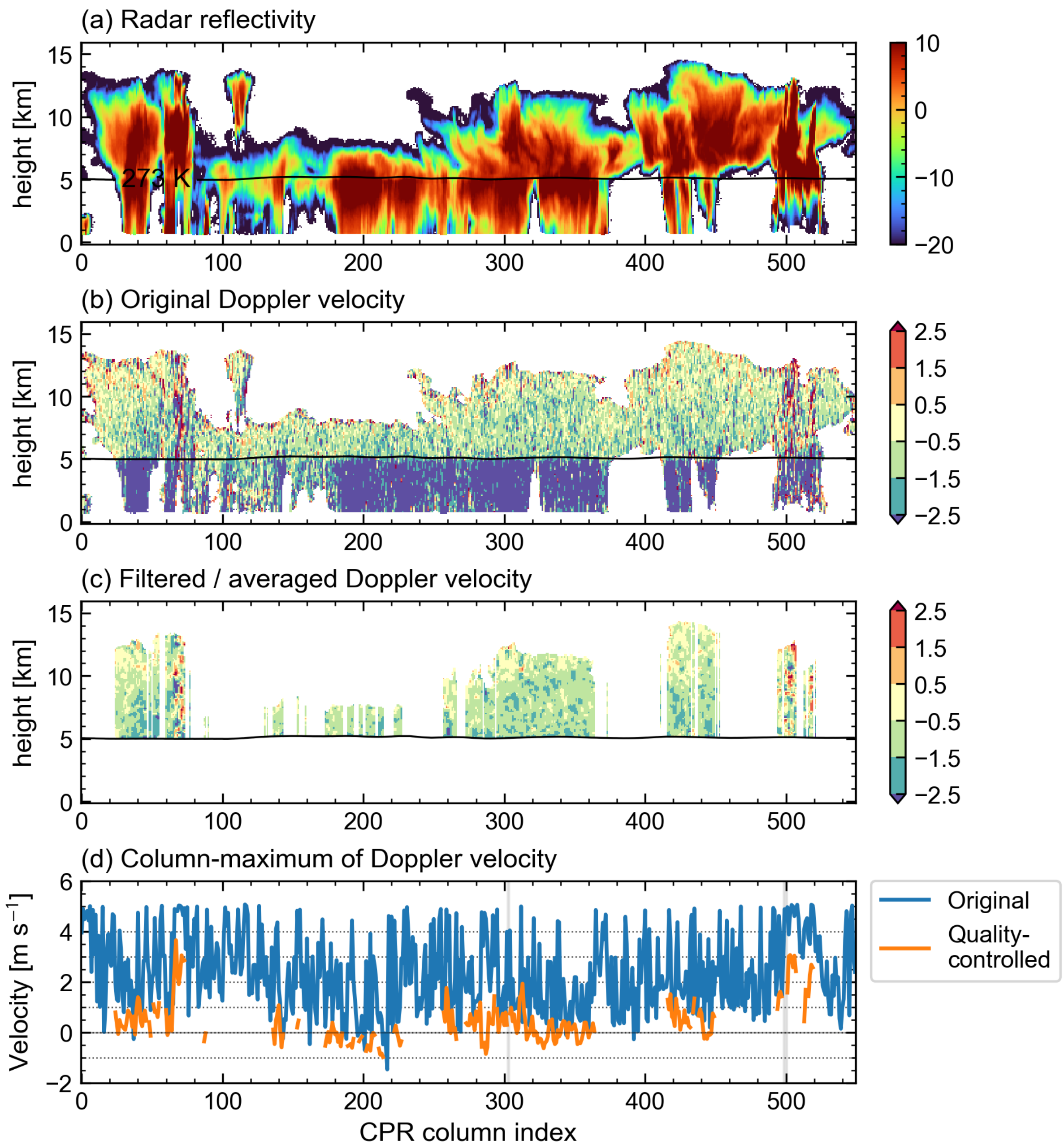

Figure 1: Example illustrating Doppler-velocity quality control and the definition of the updraft metric *MaxVd* for an EarthCARE/CPR scene. (a) Radar reflectivity factor (Ref; dBZ). (b) Native Doppler velocity (Vd; m s^{-1}) after applying only the cloud-mask threshold (cloud mask ≥ 20); positive values indicate upward motion. The black line marks the 273.15 K isotherm. (c) Doppler velocity after applying the column-selection criteria and quality control. (d) Column-maximum Doppler velocity as a function of column index, computed from the raw field in (b) (“Original”; blue) and from the filtered and averaged field in (c) (“Quality-controlled”; orange). Grey shading denotes columns flagged as being affected by residual velocity folding.

https://doi.org/10.5194/egusphere-2026-659
Preprint. Discussion started: 5 February 2026

To illustrate how the column-selection criteria, range restrictions, folding detection, and spatial averaging described in Sects. 2.2–2.4 affect the Doppler-velocity diagnostics, we examine the example case shown in Fig. 1. In the radar-reflectivity field (Fig. 1a), the cloud structure is readily identifiable. Several active convective cores with spreading anvils (column indices around 80 and 400), together with an extensive stratiform region exhibiting a bright band (column indices 180–380), are evident. Figure 1b shows the native 1 km × 200 m Doppler-velocity field with only the cloud-mask threshold (≥ 20) applied. Above the 273.15 K isotherm, indicated by the black line, the field is speckled with incoherent patches, particularly near cloud edges where reflectivity is weak. These features likely arise from random noise or small-scale turbulence rather than from coherent convective updrafts. Below the 273.15 K isotherm, although negative values are more prevalent, sporadic large positive values also appear, suggesting that strongly negative velocities may have been aliased to positive values.

Figure 1c shows the Doppler-velocity field after applying the column-selection and averaging procedures described in Sects. 2.2–2.3. The selection criteria in Sect. 2.2 remove multilayer cloud regions (column indices 80–180) and anvil regions near column indices 400 and 480. We then apply the validity filters (cloud-mask value ≥ 20, Ref > −19 dBZ, and T < 273.15 K) to Vd and average the remaining data over 3 km along track and two vertical gates (200 m), as described in Sect. 2.3. This procedure removes weak-signal outliers that are prone to error, damps small-scale turbulent fluctuations, excludes the impact of folding at temperatures warmer than 273.15 K, and yields smoother and more coherent structures.

Figure 1d compares the column-maximum Doppler velocity computed directly from the raw Vd field in Fig. 1b ("Original"; blue) with the column-maximum Doppler velocity computed from the filtered and averaged field in Fig. 1c ("Quality-controlled"; orange). Columns whose 3 km–averaged Vd profiles exhibit discrete vertical jumps with magnitudes exceeding the Nyquist velocity are flagged as folded (as described in Sect. 2.3) and are shaded in grey in Fig. 1d. The original column-maximum Vd fluctuates strongly from column to column, obscuring regime-dependent patterns, whereas the quality-controlled column-maximum Vd ($MaxVd$) varies smoothly across adjacent columns and shows distinct peaks near column indices 80, 300, 500, and 520, albeit with reduced amplitudes.

This example motivates our use of $MaxVd$, computed from the quality-controlled Vd field, as the primary updraft metric. The processing suppresses major sources of error without erasing coherent convective signals, and the modest 3 km (along-track) × 200 m (vertical) averaging increases precision while preserving the location and relative magnitude of embedded updraft cores.

3 Doppler-based identification of strong tropical convective updrafts

We identified 1,171,643 columns after applying the selection criteria described in Sect. 2.2. We then flagged columns as folded using the method described in Sect. 2.3. The analyses in Sects. 3.1–3.2 that use $MaxVd$ are restricted to non-folded columns, because in folded columns, large negative Vd values can be aliased to positive values and erroneously appear as $MaxVd$, rendering this metric unreliable. The characteristics of folded columns are assessed separately in Sect. 3.4.

https://doi.org/10.5194/egusphere-2026-659
Preprint. Discussion started: 5 February 2026

3.1 Relationship between updraft strength and vertical reflectivity structure

To examine the relationship between updraft strength, cloud development, and precipitation formation, and to evaluate the proxies used in CloudSat-based studies, we relate the updraft-intensity metric *MaxVd* to several diagnostics derived from the vertical structure of radar reflectivity.

3.1.1 Overall statistics of updrafts and their link to cloud properties

We first examine the frequency distribution of *MaxVd* for all non-folded columns to characterize its behavior and compare it with representative updraft velocities reported in previous studies (Fig. 2a). Owing to the Nyquist velocity constraint, *MaxVd* is limited to approximately +5 m s^{-1}. The distribution peaks between 0 and 1 m s^{-1}, which is smaller than typical values reported from aircraft-borne Doppler radar observations, where column-maximum updrafts often exceed 10 m s^{-1} (Heymsfield et al., 2010), as well as from cloud-top ascent rates inferred from temporal changes in infrared brightness temperature, which are on the order of 1–3 m s^{-1} (Hamada and Takayabu, 2016; Li et al., 2021). A likely reason for this apparent underestimation is the difference in the cloud life-cycle stages targeted. Whereas those previous studies primarily sampled fully developed or rapidly developing convective clouds, our statistics also include clouds in their decaying stages, thereby shifting the distribution toward weaker updrafts. In addition, the exclusion of aliased columns and the spatial averaging applied to Vd both tend to shift *MaxVd* toward smaller values. In terms of its shape, the *MaxVd* distribution exhibits clear positive skewness, with a long positive (upward) tail, consistent with previous findings (LeMone and Zipser, 1980; Lucas et al., 1994; Hamada and Takayabu, 2016). This indicates that columns with strong updrafts are relatively rare compared with those with weak or moderate updrafts.

To relate updraft strength to cloud vertical development, we construct a two-dimensional histogram of CTH versus *MaxVd* (Fig. 2b). CTH is defined as the highest altitude in a column where the cloud-mask value is ≥20. The histogram clearly shows that, as CTH increases, the mode of the *MaxVd* distribution systematically shifts toward higher values. For example, clouds with CTHs of 8–10 km exhibit a modal *MaxVd* near 0 m s^{-1}, whereas those with CTHs of 14–16 km show a mode close to 1 m s^{-1}. This pattern indicates that taller convective systems are generally more likely to contain strong updraft cores. This height dependence is qualitatively consistent with previous studies, which have reported that higher cloud tops tend to be associated with stronger convective intensity (Price and Rind, 1992; Song and Sohn, 2020).

The relationship between *MaxVd* and the column-maximum radar reflectivity (MaxRef), which is closely linked to hydrometeor size and precipitation intensity, is even more apparent (Fig. 2c). The occurrence frequency of large *MaxVd* values increases nonlinearly with increasing MaxRef, indicating that large particles are more readily generated and/or maintained in environments with relatively strong updrafts. This statistical covariation between reflectivity and updraft strength is consistent with previous observations from aircraft radars, although the absolute magnitudes depend on observational conditions, such as radar frequency (Heymsfield et al., 2010). Because of strong attenuation at 94 GHz, however, MaxRef is likely underestimated in regions with very high reflectivity (Matrosov, 2007; Kollias et al., 2022).

https://doi.org/10.5194/egusphere-2026-659
Preprint. Discussion started: 5 February 2026

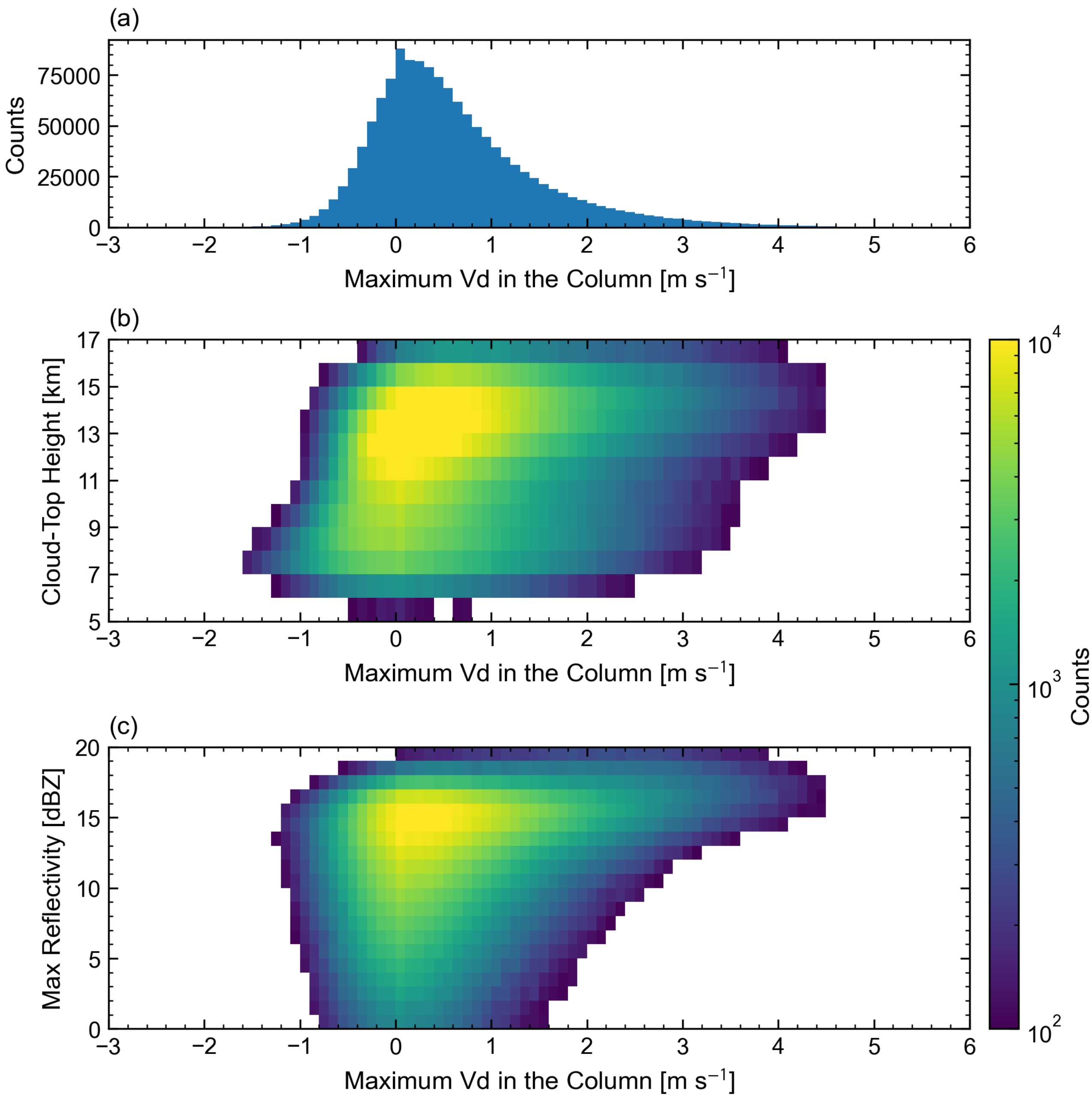

Figure 2: Statistical distribution of the Doppler-derived updraft metric (*MaxVd*) and its relationship to cloud vertical development and precipitation intensity for all analyzed non-folded tropical columns. (a) Histogram of *MaxVd* (m s^{-1}). (b) Two-dimensional histogram of *MaxVd* versus cloud-top height. (c) Two-dimensional histogram of *MaxVd* versus column-maximum radar reflectivity (*MaxRef*; dBZ). Shading in (b) and (c) indicates sample counts (logarithmic color scale); only bins with ≥ 100 samples are shown.

https://doi.org/10.5194/egusphere-2026-659
Preprint. Discussion started: 5 February 2026

3.1.2 Vertical structure of reflectivity depending on updraft strength

To further investigate the vertical structure of radar reflectivity, we classified the columns into two categories based on their *MaxVd*. Strong-updraft (SU) columns are defined as those with *MaxVd* > 2.5 m s⁻¹, totaling 75,449 columns (6.66% of all non-folded columns). The remaining non-folded columns are classified as non-SU (NonSU). This threshold isolates a relatively rare but dynamically distinct subset of strong-updraft cases.

We then use normalized Contoured Frequency-by-Altitude Diagrams (normalized CFADs; Luo et al., 2009) to compare the statistical distributions of reflectivity profiles for the two categories (Fig. 3). The normalized CFADs reveal clear structural contrasts between SU and NonSU columns. SU columns exhibit a significantly larger fraction of high-reflectivity bins (≥10 dBZ) at high altitudes (>8 km), indicating that strong updrafts loft large hydrometeors deep into the upper troposphere. The observed Doppler velocity (Vd) is the sum of the particle fall speed and the vertical motion of the ambient air. Because greater radar reflectivity generally corresponds to faster particle fall speeds (Seiki et al., 2025, submitted), which act to reduce Vd, the occurrence of high reflectivity at high altitudes in SU columns implies particularly strong updrafts. Below the melting layer (<5 km), by contrast, reflectivity in SU is smaller than in NonSU, likely due to stronger radar attenuation, a feature consistent with previous studies (Luo et al., 2014).

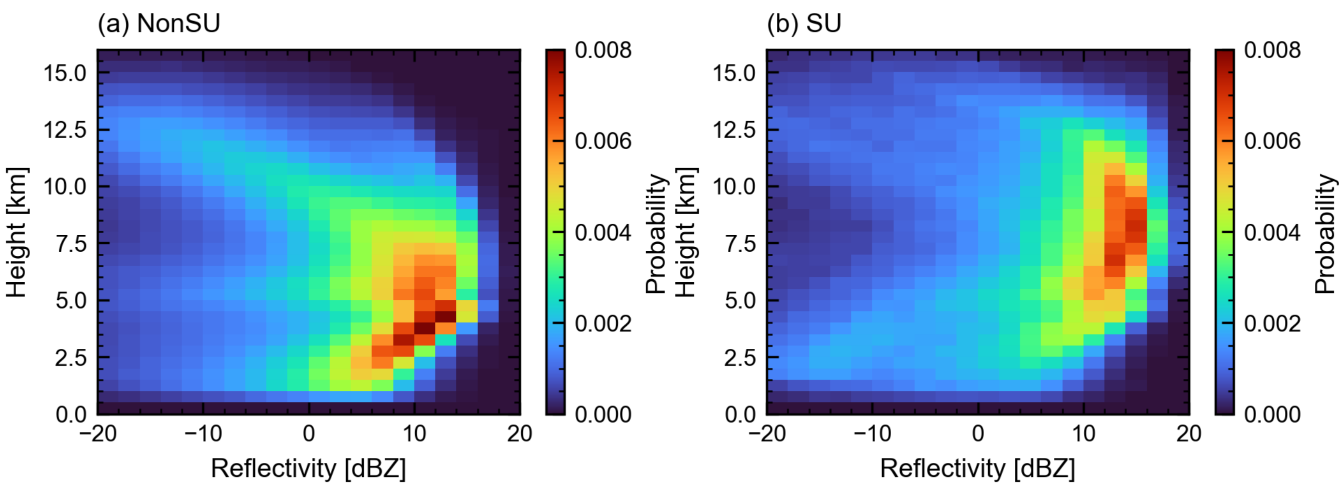

Figure 3: Normalized contoured frequency-by-altitude diagrams (CFADs) of EarthCARE/CPR radar reflectivity (Ref; dBZ) for (a) non–strong-updraft (NonSU) columns and (b) strong-updraft (SU) columns, where SU is defined by a column-maximum Doppler velocity of *MaxVd* > 2.5 m s⁻¹. Reflectivity is binned in 2 dBZ intervals, and the vertical coordinate is binned in 500 m intervals. Each panel is normalized by its total sample count such that the color indicates probability (i.e., the sum over all bins in each panel equals 1).

3.1.3 Relationship between CTH, ETH, and Updraft Strength

https://doi.org/10.5194/egusphere-2026-659
Preprint. Discussion started: 5 February 2026

This structural difference in reflectivity between the SU and NonSU columns is further quantified using box-and-whisker plots of various height metrics (Fig. 4). The median CTH of SU columns is approximately 900 m higher than that of NonSU columns. The contrast is even more pronounced for ETH at higher reflectivity thresholds. The median ETH at 0 dBZ, denoted as ETH(0), is approximately 2.6 km higher in SU columns, while the median ETH at 10 dBZ, denoted as ETH(10), is approximately 3.0 km higher. The substantially larger difference in ETH compared with CTH indicates that ETH is a more direct and sensitive proxy for updraft strength than CTH.

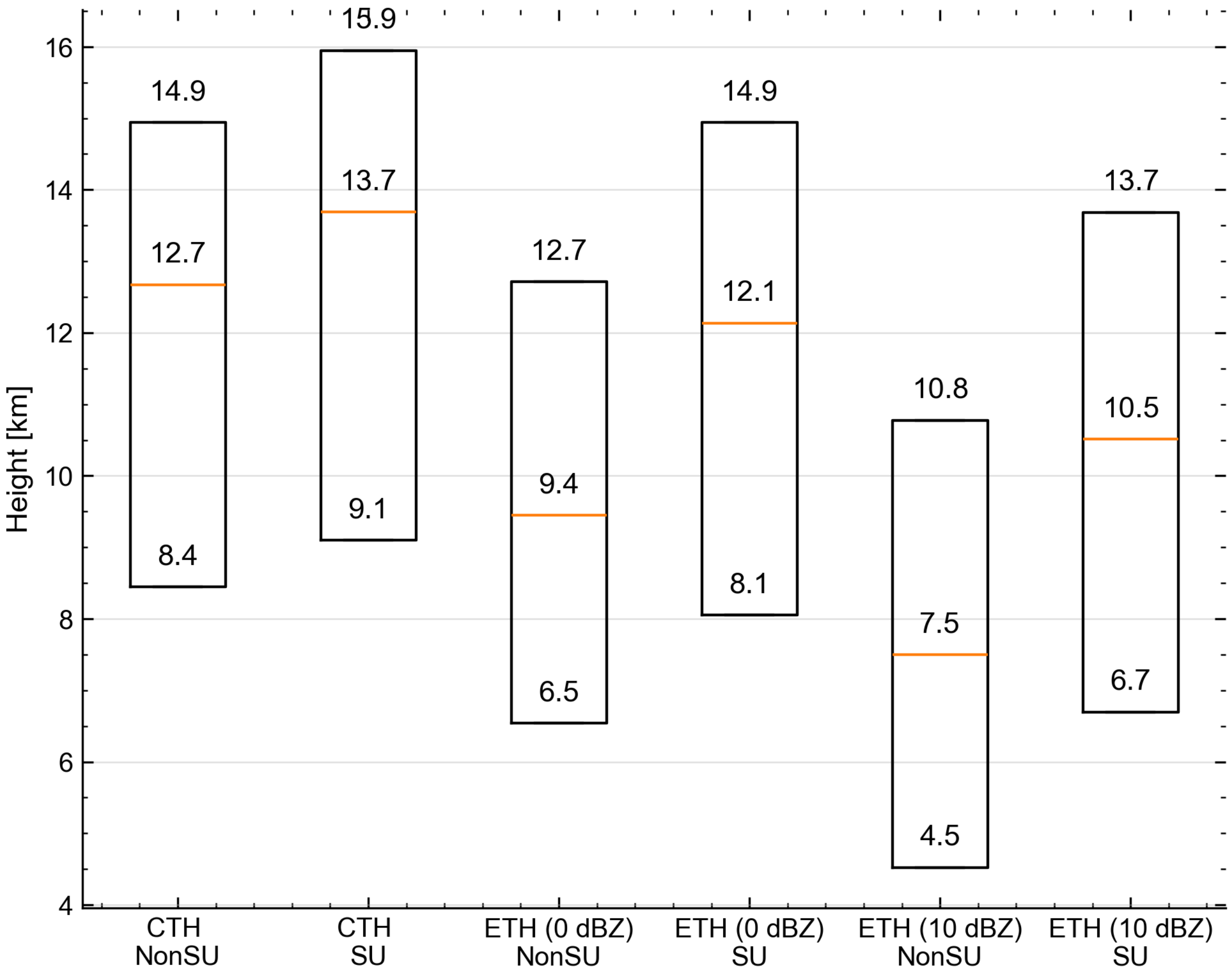

Figure 4: Box-and-whisker summaries of cloud vertical extent for non–strong-updraft (NonSU) and strong-updraft (SU) columns, shown for cloud-top height (CTH) and echo-top heights at reflectivity thresholds of 0 and 10 dBZ [ETH(0) and ETH(10)]. For each metric, the box spans the 10th–90th percentiles and the central line indicates the median (50th percentile). Numeric labels denote the 10th, 50th, and 90th percentile heights (km).

To further explore the interplay between these height-based metrics, we examine the joint distributions of CTH and ETH(0) separately for NonSU (Fig. 5b) and SU columns (Fig. 5e). Because ETH(0) is, by definition, equal to or lower than CTH, the

https://doi.org/10.5194/egusphere-2026-659
Preprint. Discussion started: 5 February 2026

populated region in the CTH–ETH(0) plane is confined to the triangular area above the 1:1 line. For both SU and NonSU columns, ETH(0) and CTH are strongly and positively correlated, consistent with previous satellite- and radar-based studies that have related differences between cloud-top and precipitation-top heights to convective intensity and life-cycle stage (e.g., Masunaga et al., 2005; Masunaga and Kummerow, 2006; Kikuchi and Suzuki, 2019). However, their detailed characteristics differ markedly. NonSU columns are, on average, shallower and exhibit a broad distribution with a large separation between ETH(0) and CTH. In contrast, SU columns are systematically taller, and their joint distribution lies much closer to the 1:1 line, indicating a smaller gap between ETH(0) and CTH.

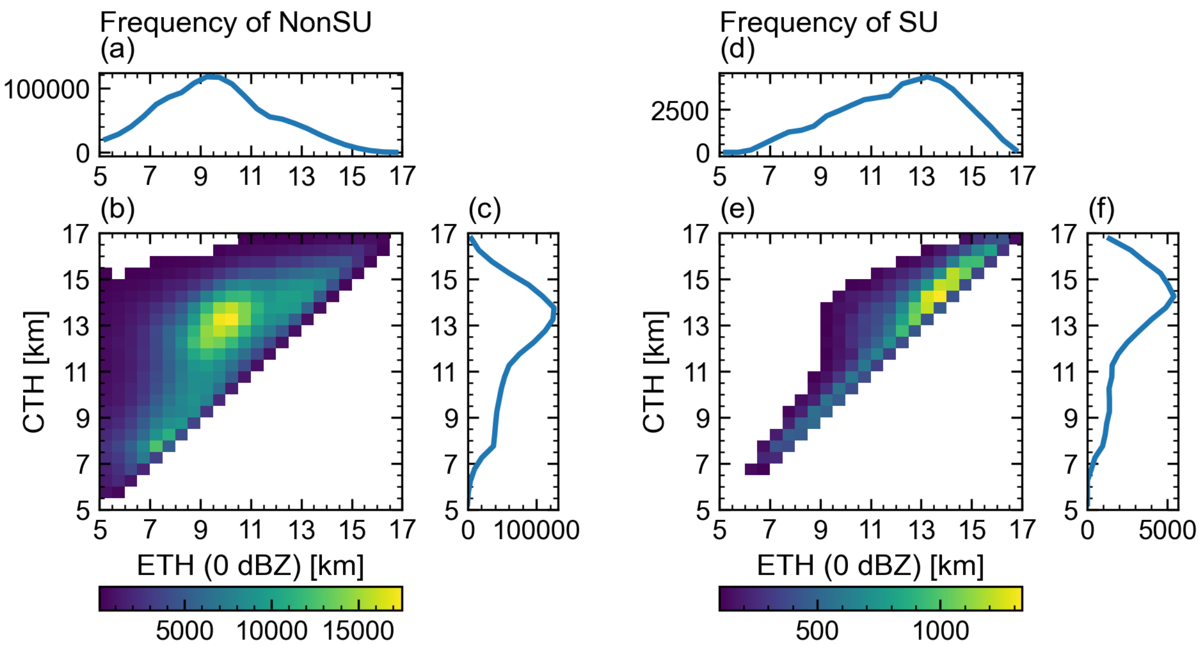

Figure 5: Relationship between cloud-top height (CTH) and the 0 dBZ echo-top height [ETH(0)] for non–strong-updraft (NonSU) and strong-updraft (SU) columns. Two-dimensional histograms of CTH versus ETH(0) are shown for (b) NonSU and (e) SU; shading indicates sample counts per bin, and only bins with ≥ 100 samples are colored. The corresponding marginal distributions are shown for ETH(0) in (a) NonSU and (d) SU, and for CTH in (c) NonSU and (f) SU.

Building on Fig. 5, Fig. 6 further quantifies how the probability of SU occurrence varies with CTH and ETH(0), thereby more clearly characterizing the distinct nature of SU columns. The SU ratio (defined as the number of SU columns divided by the total number of columns, i.e., SU plus NonSU) increases monotonically with CTH (Fig. 6c), remaining below 0.05 for shallow clouds (CTH $\lesssim$ 8 km) and approaching 0.10 for the tallest clouds (CTH $\gtrsim$ 16 km). A similar but even sharper increase is observed for ETH(0): the SU ratio rises monotonically with ETH(0) (Fig. 6a), from below 0.03 for ETH(0) $\lesssim$ 7 km to more than 0.30 for ETH(0) $\gtrsim$ 15 km.

The two-dimensional map of the SU ratio (Fig. 6b) shows that the likelihood of SU occurrence increases jointly with CTH and ETH(0) and is maximized in the upper-right region of the ETH(0)–CTH phase space, that is, for tall cloud systems in which

https://doi.org/10.5194/egusphere-2026-659
Preprint. Discussion started: 5 February 2026

ETH(0) approaches CTH. For a fixed CTH, bins with larger ETH(0) exhibit higher SU fractions, indicating a clear dependence on the separation between CTH and ETH(0). Conversely, when the separation between ETH(0) and CTH is large (i.e., far from the 1:1 line), SU occurrence is strongly suppressed. Notably, even at moderate CTH (CTH < 10 km), columns with small CTH–ETH(0) separation still show a substantial probability of being classified as SU. This suggests that a steep reflectivity gradient near the cloud top is a strong indicator of vigorous updrafts. This behavior directly addresses a historical blind spot in proxy climatologies of intense convection, which often impose reflectivity thresholds at high altitudes and therefore overlook low-topped convective columns (Zipser et al., 2006; Romatschke et al., 2010; Liu and Zipser, 2015).

These results highlight the importance of the separation between CTH and ETH(0). We therefore define $\Delta H \equiv CTH - ETH(0)$ as a compact diagnostic that links dynamics and microphysics. Small ΔH corresponds to the presence of large particles near the cloud top in developing convective cores, whereas large ΔH characterizes decaying or weakly forced columns in which larger hydrometeors are confined to lower levels. This interpretation is consistent with conceptual models of convective evolution and with CloudSat-based intensity proxies that emphasize small CTH–ETH(0) separation (Takahashi and Luo, 2014); however, it is here validated using direct Doppler velocity measurements and extended to low-topped convective populations.

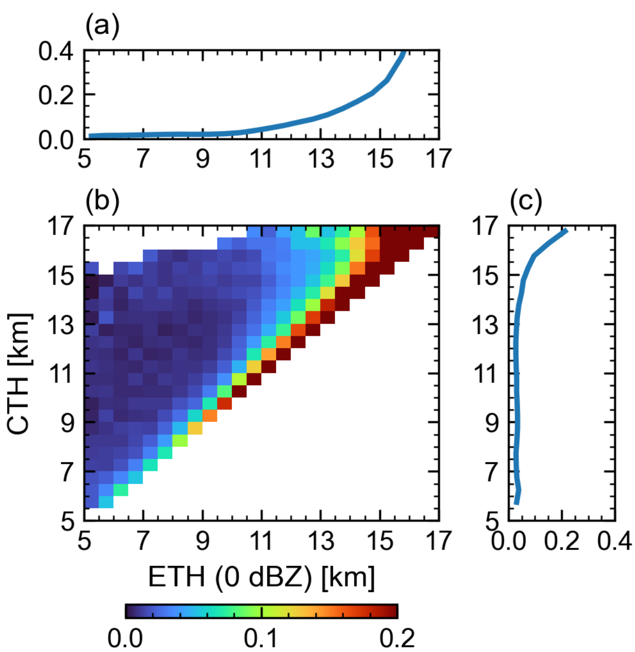

Figure 6: Occurrence ratio of strong-updraft (SU) columns as a function of the 0 dBZ echo-top height [ETH(0)] and cloud-top height (CTH). The SU ratio is defined as the number of SU columns divided by the total number of columns (SU + NonSU) within each bin. (a) Marginal SU ratio as a function of ETH(0). (b) Two-dimensional distribution of the SU ratio in the CTH–ETH(0) phase space; colors indicate the SU fraction. White areas denote bins with no data. (c) Marginal SU ratio as a function of CTH.

https://doi.org/10.5194/egusphere-2026-659
Preprint. Discussion started: 5 February 2026

3.2 Spatial and diurnal characteristics

3.2.1 Spatial and diurnal pattern of strong updraft column

To place the column-wise updraft statistics in a geographical and diurnal context, we analyze where and when strong-updraft columns (SU; $MaxVd > 2.5$ m s^{-1}) occur at two local times (02:00 and 14:00 LT) and how their occurrence relates to regional cloud structure. We begin by examining the spatial distribution of all non-folded columns within the analysis domain (Fig. 7a). These columns are predominantly concentrated over well-known hotspots of deep convection (Zipser et al., 2006; Liu and Zipser, 2015), including the eastern Pacific Intertropical Convergence Zone (EPAC-ITCZ), the Amazon basin, central Africa, the Maritime Continent, and the South Pacific Convergence Zone (SPCZ), and are relatively sparse over the subtropical oceans. This geographical pattern confirms that our procedure effectively isolates columns embedded within convective cloud systems. We define five large-sample regions (Fig. 7a): the EPAC-ITCZ (5–15° N, 150–90° W), central Africa (15° S–15° N, 10–40° E), the Amazon basin (20° S–8° N, 80–45° W), the Maritime Continent (15° S–15° N, 90–160° E), and the SPCZ, approximated by a triangle with vertices at (0° N, 165° E), (20° S, 165° E), and (30° S, 120° W). These regions are used throughout the subsequent analysis to quantify regional differences in the occurrence and structure of SU columns.

The SU fraction, defined as the ratio of SU columns to all non-folded columns within each 2.5° × 2.5° grid box, exhibits pronounced regional contrasts (Fig. 7b). In most grid boxes, the SU fraction is below 0.10, and only a small number of boxes exceed 0.15. Local maxima are generally collocated with regions of intense continental convection over central Africa and the Amazon basin, whereas the Maritime Continent exhibits comparatively lower SU fractions. Representative values for convectively active regions are summarized in Table 1, highlighting an enhancement over continental regions (Amazon: 5.3%, central Africa: 5.9%) relative to oceanic convective zones (EPAC-ITCZ: 4.6%, Maritime Continent: 3.8%, SPCZ: 4.2%).

https://doi.org/10.5194/egusphere-2026-659
Preprint. Discussion started: 5 February 2026

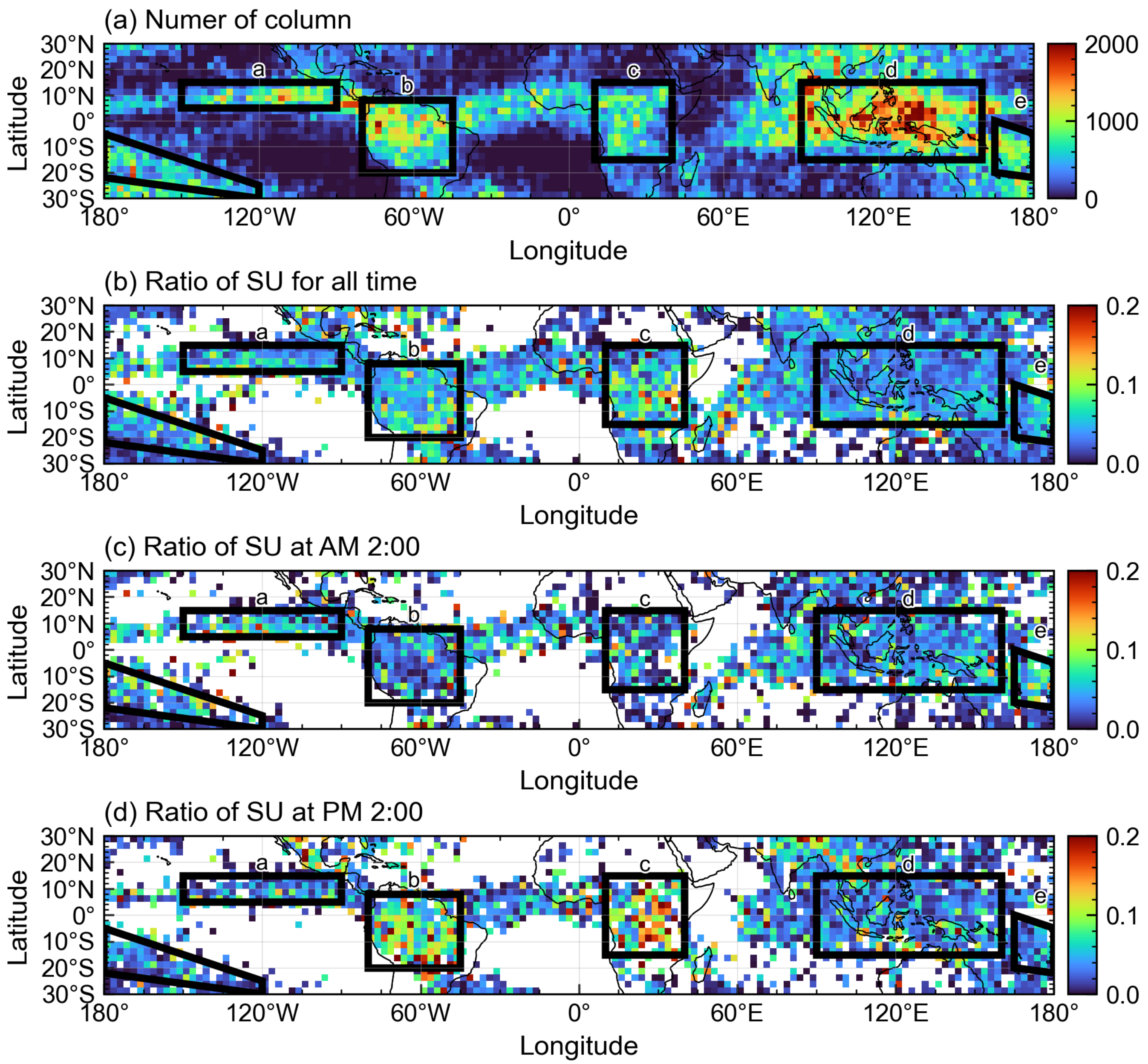

Figure 7: Spatial distribution of the analyzed columns and the occurrence of strong-updraft (SU) columns. (a) Number of selected non-folded columns per 2.5° × 2.5° grid box over 30°S–30°N. (b) Fraction of SU columns (*MaxVd* > 2.5 m s^{-1}) relative to all non-folded columns in each grid box. (c–d) Same as (b), but separated by local overpass time: (c) late night (~02:00 LT; ascending node) and (d) early afternoon (~14:00 LT; descending node). Grid boxes with fewer than 100 total columns are masked in (b–d). Black rectangles labeled a–e indicate the regions used for the regional analyses (EPAC–ITCZ, Amazon, central Africa, Maritime Continent, and SPCZ).

https://doi.org/10.5194/egusphere-2026-659
Preprint. Discussion started: 5 February 2026

When the statistics are separated by local overpass time—late night (ascending node, around 02:00 LT) versus early afternoon (descending node, around 14:00 LT)—the regional contrast becomes clearer (Figs. 7c–d, Table 1). Over the Maritime Continent, the EPAC-ITCZ, and the SPCZ, SU fractions are slightly higher at night than in the early afternoon. In contrast, central Africa and the Amazon basin exhibit a pronounced daytime enhancement, with early-afternoon SU fractions of 9.3% and 8.1%, respectively, nearly twice the tropical-mean value of 4.3% computed across all regions and local times. This geographical and diurnal pattern is consistent with prior satellite-based characterizations using other convective-intensity metrics, such as echo-top height (ETH) and lightning flash rate (Nesbitt and Zipser, 2003; Christian et al., 2003; Liu and Zipser, 2005; Zipser et al., 2006; Liu et al., 2008; Cecil et al., 2014; Pilewskie and L'Ecuyer, 2022).

3.2.2 Structural origin of regional and diurnal contrasts

What differences in cloud properties account for the particularly elevated early-afternoon SU fractions over central Africa and the Amazon, while remaining modest in other convective regions (Sect. 3.2.1; Table 1)? Guided by the column-wise radar-reflectivity structural analysis in Sect. 3.1, we address this question by examining the median CTH, ETH(0), and their separation, $\Delta H \equiv \mathrm{CTH} - \mathrm{ETH}(0)$. In addition, we consider a simple morphology metric—the cloud length—defined as the along-track length of contiguous cloudy segments.

As summarized in Table 2, clouds over central Africa and the Amazon during the early afternoon do not stand out as being exceptionally tall. The tropical-mean median CTH across all columns and local times is 12.7 km, compared with 12.1 km over central Africa and 12.8 km over the Amazon at 14:00 LT. Similarly, the median ETH(0) is 9.5 km in the tropical mean and 9.1 km and 9.8 km over central Africa and the Amazon, respectively, during the early afternoon. These values are comparable to, or even slightly lower than, those in other convective regions, such as the Maritime Continent, the EPAC-ITCZ, and the SPCZ. Thus, the enhanced SU fractions in continental afternoon regimes cannot be explained simply by systematically higher cloud or echo tops.

Instead, the most distinctive feature of early-afternoon convection over central Africa and the Amazon is a markedly smaller ΔH. The tropical-mean median ΔH across all local times is 2.4 km, whereas it is only 1.9 km over central Africa and the Amazon during the afternoon—smaller than in any other region–local-time combination listed in Table 2. By contrast, the Maritime Continent and the SPCZ exhibit substantially larger ΔH values (3.0 km and 2.9 km, respectively, at 14:00 LT). A complementary perspective is obtained by comparing the median ΔH with the difference between the median CTH and median ETH(0). For the tropics as a whole, the median ΔH is 2.4 km, whereas the difference between the median CTH and median ETH(0) is 3.2 km. The contrast is even more pronounced for afternoon central Africa and the Amazon, for which the corresponding values are 1.9 km and 3.0 km. These comparisons indicate that the ΔH distributions are skewed toward small values and that clouds with small CTH–ETH(0) separation occupy a disproportionately large fraction of the population, with this tendency being particularly pronounced in early-afternoon convection over central Africa and the Amazon.

https://doi.org/10.5194/egusphere-2026-659
Preprint. Discussion started: 5 February 2026

Horizontal cloud length, summarized in Table 2, provides an additional clue to the nature of the underlying convective systems. The tropical-mean median cloud length is 482 km, but it is only 283 km and 294 km over central Africa and the Amazon, respectively, during the early afternoon. In contrast, the SPCZ and the Maritime Continent exhibit substantially larger median cloud lengths (567 km and 504 km, respectively, at 14:00 LT). These statistics suggest that early-afternoon convection over central Africa and the Amazon is dominated by relatively compact systems, whereas oceanic regions—especially the SPCZ and the Maritime Continent—more frequently host large, organized systems.

To further characterize regional differences in the CTH–ETH(0) relationship, we examine deviations of the two-dimensional histograms of CTH versus ETH(0) from a tropics-wide reference distribution (constructed by combining all regions and local times), as shown in Fig. 8a–c. For early-afternoon convection over central Africa and the Amazon, the difference maps indicate a reduced occurrence of stratiform-like profiles characterized by large ΔH, together with an enhanced occurrence of profiles exhibiting small ΔH and moderate-to-high cloud tops (CTH ≈ 6–15 km). When considered alongside the relatively short cloud lengths, these features indicate a cloud population skewed toward developing or mature convective columns, rather than decaying systems with extensive stratiform regions.

We next examine in greater detail how these structural differences relate to the enhanced occurrence of SU columns. To this end, we analyze deviations in the SU fraction as a function of CTH and ETH(0) from the tropical-mean distribution (cf. Fig. 6), as shown in Figs. 9a–c. Over early-afternoon convection in central Africa and the Amazon, the SU fraction is enhanced across much of the (CTH, ETH(0)) phase space, with particularly strong positive anomalies along and near the 1:1 line, where ΔH is small. In other words, columns with small CTH–ETH(0) separation are both more common and more likely to host strong updrafts than in the tropical mean. The elevated regional SU fractions therefore arise from a combination of (i) a shift in the underlying cloud population toward small-ΔH structures and (ii) an increased probability that a given small-ΔH column contains strong Doppler updrafts, rather than from an overall increase in extremely tall clouds.

The Maritime Continent provides a useful contrast. Despite having relatively high median CTH and ETH(0), comparable to or exceeding those over central Africa and the Amazon (Table 2), SU fractions over the Maritime Continent remain close to or slightly below the tropical mean and are therefore substantially lower than those over these continental regions (Table 1). Structurally, clouds over the Maritime Continent tend to exhibit larger ΔH and longer horizontal extents, indicating a greater prevalence of deep convective systems with broad stratiform regions. This pattern is also evident in Fig. 8c, which shows an enhanced frequency of clouds with high CTH but relatively low ETH(0). Furthermore, the SU fraction at a given (CTH, ETH(0)) pair (Fig. 9c) tends to be somewhat suppressed for developing clouds with moderate CTH and small ΔH, conditions under which strong updrafts are more common over central Africa and the Amazon. The combined effects of more frequent stratiform profiles and a reduced SU fraction during the developing stage therefore lead to overall smaller SU fractions over the Maritime Continent.

These regional patterns are consistent with previous satellite-based analyses of deep convective intensity across the three major tropical "chimney zones," which show that convection over tropical Africa exhibits the strongest updrafts, Amazonia is intermediate, and the tropical warm-pool/Maritime Continent regime displays the weakest convective intensity when measured

https://doi.org/10.5194/egusphere-2026-659
Preprint. Discussion started: 5 February 2026

using radar echo-top heights and related proxies (e.g., Takahashi and Luo, 2014; Takahashi et al., 2017, 2023; Liu et al., 2007; Zipser et al., 2006). These studies argue that stronger land convection arises from a more efficient conversion of convective available potential energy into vertical kinetic energy, associated with deeper and drier boundary layers and higher lifting condensation levels, which produce broader and more buoyant convective cores that are less susceptible to dilution by entrainment. In contrast, convection over the warm-pool/Maritime Continent regime tends to exhibit narrower cores and larger entrainment rates, resulting in weaker updrafts (Lucas et al., 1994; Williams and Stanfill, 2002; Takahashi et al., 2017, 2023). Our results support these findings by showing the same regional ordering of convective intensity based on direct Doppler velocity measurements. Furthermore, by analyzing radar reflectivity and Doppler velocity as independent variables, we demonstrate clear regional differences in updraft strength in developing-stage clouds characterized by moderate-to-high CTH and small CTH–ETH(0) separation.

Table 1: Regional occurrence of strong-updraft (SU) columns. For each domain and local overpass time (≈02:00 and ≈14:00 LT), the table lists the total number of selected non-folded cloud columns, the number of columns classified as SU (*MaxVd* > 2.5 $m\ s^{-1}$), and the resulting SU ratio (%). "ALL" denotes the tropical aggregate (30°S–30°N). Region definitions are shown in Fig. 7a (see Sect. 3.2.1).

	Local Time	ALL	Central Africa	Amazon	Maritime Continent	EPAC-ITCZ	SPCZ
	All	1.20E+06	6.27E+04	1.04E+05	2.93E+05	5.38E+04	8.30E+04
	02:00 LT	6.29E+05	3.78E+04	6.29E+04	1.52E+05	2.59E+04	4.20E+04
Total Count	14:00 LT	5.74E+05	2.49E+04	4.12E+04	1.41E+05	2.79E+04	4.09E+04
	All	5.12E+04	3.68E+03	5.54E+03	1.12E+04	2.47E+03	3.51E+03
	02:00 LT	2.55E+04	1.36E+03	2.19E+03	6.05E+03	1.47E+03	2.11E+03
SU count	14:00 LT	2.57E+04	2.32E+03	3.35E+03	5.16E+03	1.01E+03	1.39E+03
	All	4.3%	5.9%	5.3%	3.8%	4.6%	4.2%
	02:00 LT	4.1%	3.6%	3.5%	4.0%	5.6%	5.0%
SU ratio	14:00 LT	4.5%	9.3%	8.1%	3.7%	3.6%	3.4%

Table 2: Regional median structural metrics. Regional medians of cloud-top height (CTH; km), 0 dBZ echo-top height [ETH(0); km], their separation ΔH ≡ CTH − ETH(0) (km), and along-track cloud length (km) for the tropical aggregate and five convective regions (central Africa, Amazon, Maritime Continent, EPAC–ITCZ, and SPCZ), stratified by local overpass time (All, ≈02:00 LT, and ≈14:00 LT). Region definitions are shown in Fig. 7a (see Sect. 3.2.1).

	Local Time	ALL	Central Africa	Amazon	Maritime Continent	EPAC-ITCZ	SPCZ
	All	12.7	12.2	12.6	13.4	13.0	13.0
cloud top height	02:00 LT	12.6	12.3	12.4	13.3	13.0	13.0

https://doi.org/10.5194/egusphere-2026-659
Preprint. Discussion started: 5 February 2026

	14:00 LT	12.8	12.1	12.8	13.5	12.9	13.0
	All	9.5	8.9	9.4	9.9	10.0	9.7
	02:00 LT	9.4	8.8	9.0	9.9	10.2	9.9
echo (0 dBZ) top height	14:00 LT	9.6	9.1	9.8	9.9	9.9	9.6
	All	2.4	2.3	2.3	2.7	2.3	2.7
	02:00 LT	2.3	2.5	2.5	2.5	2.0	2.4
cloud - echo (0 dBZ)	14:00 LT	2.5	1.9	1.9	3.0	2.5	2.9
	All	482	418	416	503	472	560
	02:00 LT	495	516	534	500	449	557
cloud length	14:00 LT	468	283	294	504	484	567

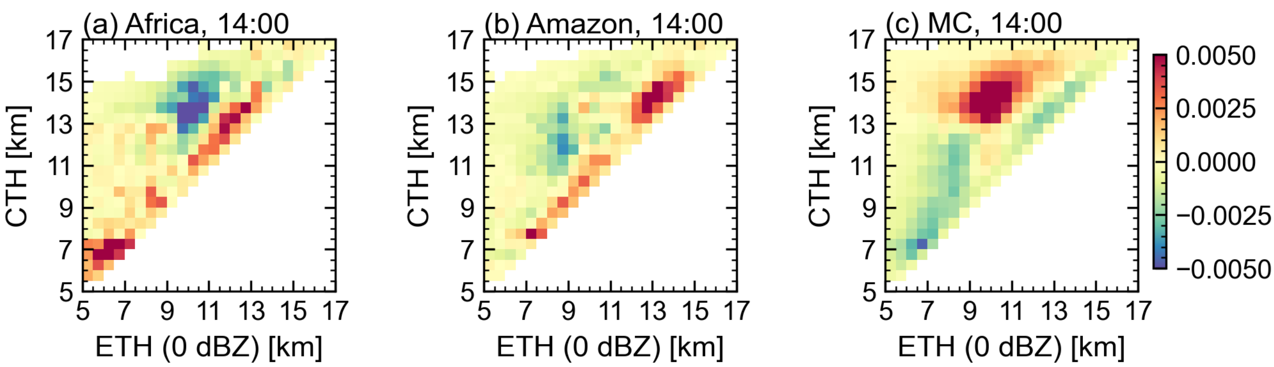

Figure 8: Deviations in the joint probability density function (PDF) of cloud-top height (CTH) and the 0 dBZ echo-top height [ETH(0)] relative to the tropics-wide reference distribution (all regions and local times combined; non-folded columns only). Panels show early afternoon (~14:00 LT) convection over (a) central Africa, (b) the Amazon, and (c) the Maritime Continent. Bin size is 0.5 km in both dimensions; only bins with N ≥ 100 columns are shown.

https://doi.org/10.5194/egusphere-2026-659
Preprint. Discussion started: 5 February 2026

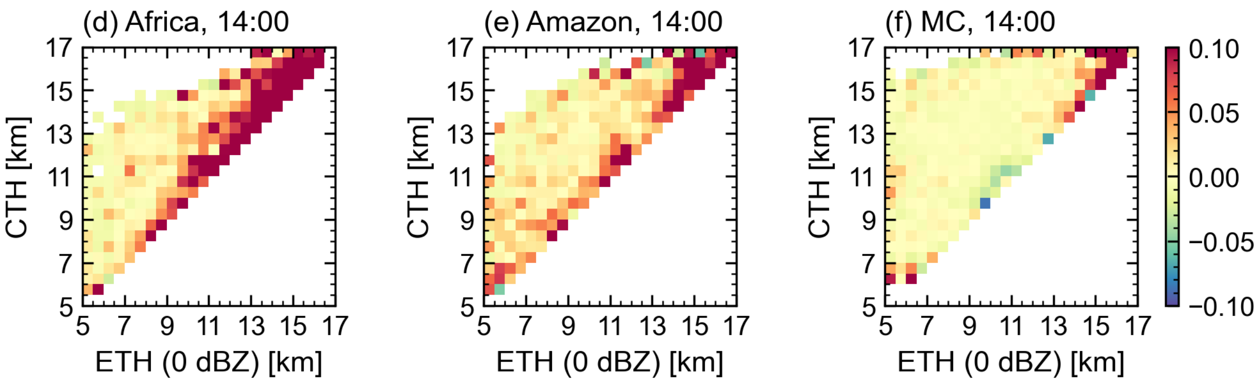

Figure 9: Deviations in the SU fraction conditioned on cloud-top height (CTH) and the 0 dBZ echo-top height [ETH(0)] relative to the tropics-wide conditioned SU fraction (as in Fig. 6b). Panels show early afternoon (~14:00 LT) convection over (a) central Africa, (b) the Amazon, and (c) the Maritime Continent. Bin size is 0.5 km in both dimensions; only bins with N ≥ 100 columns are shown.

3.3 Implication from Doppler-velocity folding

In Sects. 3.1–3.2, our analysis was restricted to non-folded columns to ensure robust quantitative statistics of Doppler-derived updraft strength. In this subsection, we shift focus to columns in which Doppler-velocity folding (aliasing) is detected. Previous Doppler-radar studies have shown that the most intense convective cores often generate radial velocities exceeding the instrument Nyquist limit, resulting in folded spectra and aliased velocity measurements (Battaglia et al., 2011; Kollias et al., 2014; Sy et al., 2014). Although these folded velocities cannot be used directly as quantitative estimates of updraft magnitude, the presence of velocity folding itself provides a qualitative indicator of extreme vertical motions (Galfione et al., 2025).

After applying the column-selection and Doppler quality-control procedures described in Sects. 2.2–2.3, we identify 38,235 columns (3.2% of the total 1,394,477 columns) as exhibiting at least one folding (aliasing) event, whereas 1,133,408 columns (96.74%) show no evidence of folding. To relate velocity folding to cloud properties, we compute the folded-column fraction as a function of cloud-top height (CTH) and the 0-dBZ echo-top height, ETH(0) (Fig. 10). The resulting pattern closely mirrors the structural relationships documented for strong updrafts in Sect. 3.1 (cf. Fig. 6): the folding fraction increases systematically with both CTH and ETH(0) and becomes particularly large when $\Delta H \equiv CTH - ETH(0)$ is small. This behavior indicates that folding preferentially occurs in structures most likely to host intense updrafts.

The geographical and diurnal characteristics of folding further support this interpretation. Fig. 11 shows the spatial distribution of the fraction of columns exhibiting at least one folding event, and Table 3 summarizes the corresponding regional and local-time statistics. In the tropical mean, the folding fraction is 3.2%, increasing modestly from the nighttime overpass (02:00 LT; 2.9%) to the early afternoon overpass (14:00 LT; 3.6%). Continental regions characterized by vigorous afternoon convection stand out: over central Africa and the Amazon, folding fractions averaged over all local times reach 4.9% and 4.2%, respectively, and increase to 8.8% and 7.3% during the 14:00 LT overpass, compared with only 2.3% and 1.9% at 02:00 LT (Table 3). In contrast, oceanic convergence zones such as the Maritime Continent, EPAC-ITCZ, and SPCZ exhibit smaller

https://doi.org/10.5194/egusphere-2026-659
Preprint. Discussion started: 5 February 2026

folding fractions of around 3% and a much weaker diurnal contrast. These regional and diurnal patterns closely parallel those of strong-updraft columns (SU) discussed in Sect. 3.2. Afternoon continental regions (central Africa and the Amazon) show concurrent enhancements in both the SU fraction (Table 1) and the folding fraction (Table 3), whereas oceanic regions remain relatively muted in both diagnostics.

In terms of radar reflectivity structure, as well as geographical and diurnal characteristics, folded columns exhibit trends that are largely consistent with those identified for non-folded SU columns. Taken together, this consistency suggests that Doppler folding, despite arising from a measurement limitation, serves as a useful qualitative tracer of environments that favor extreme updrafts. In particular, the co-location of high folding fractions with tall, small-ΔH columns in early-afternoon continental convection reinforces the interpretation that such structures are strongly associated with the most intense convective cores sampled by EarthCARE/CPR.

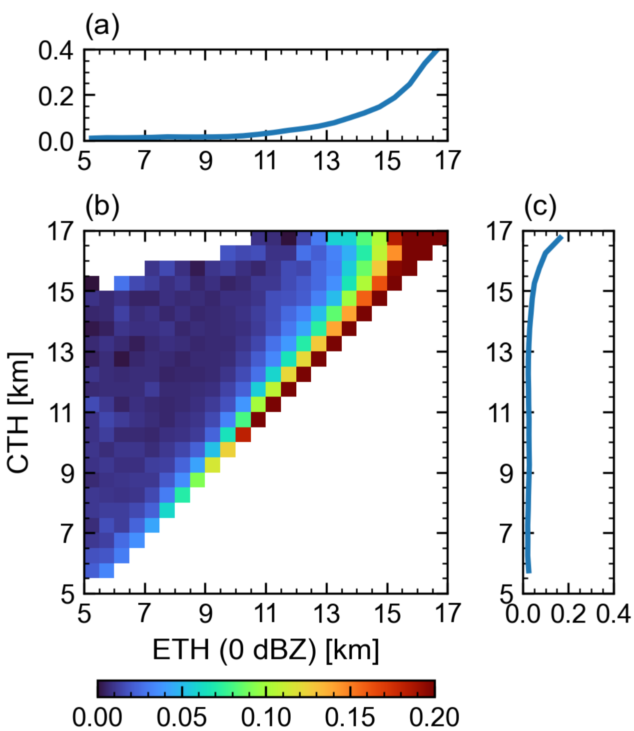

Figure 10: Fraction of columns affected by Doppler-velocity folding (aliasing) as a function of cloud-top height (CTH) and the 0 dBZ echo-top height, ETH(0). The folding ratio is defined as the number of columns with at least one detected folding event divided by the total number of selected columns within each bin. (b) Two-dimensional distribution of the folding ratio in the CTH–ETH(0) plane. (a) Marginal folding ratio as a function of ETH(0). (c) Marginal folding ratio as a function of CTH.

https://doi.org/10.5194/egusphere-2026-659
Preprint. Discussion started: 5 February 2026

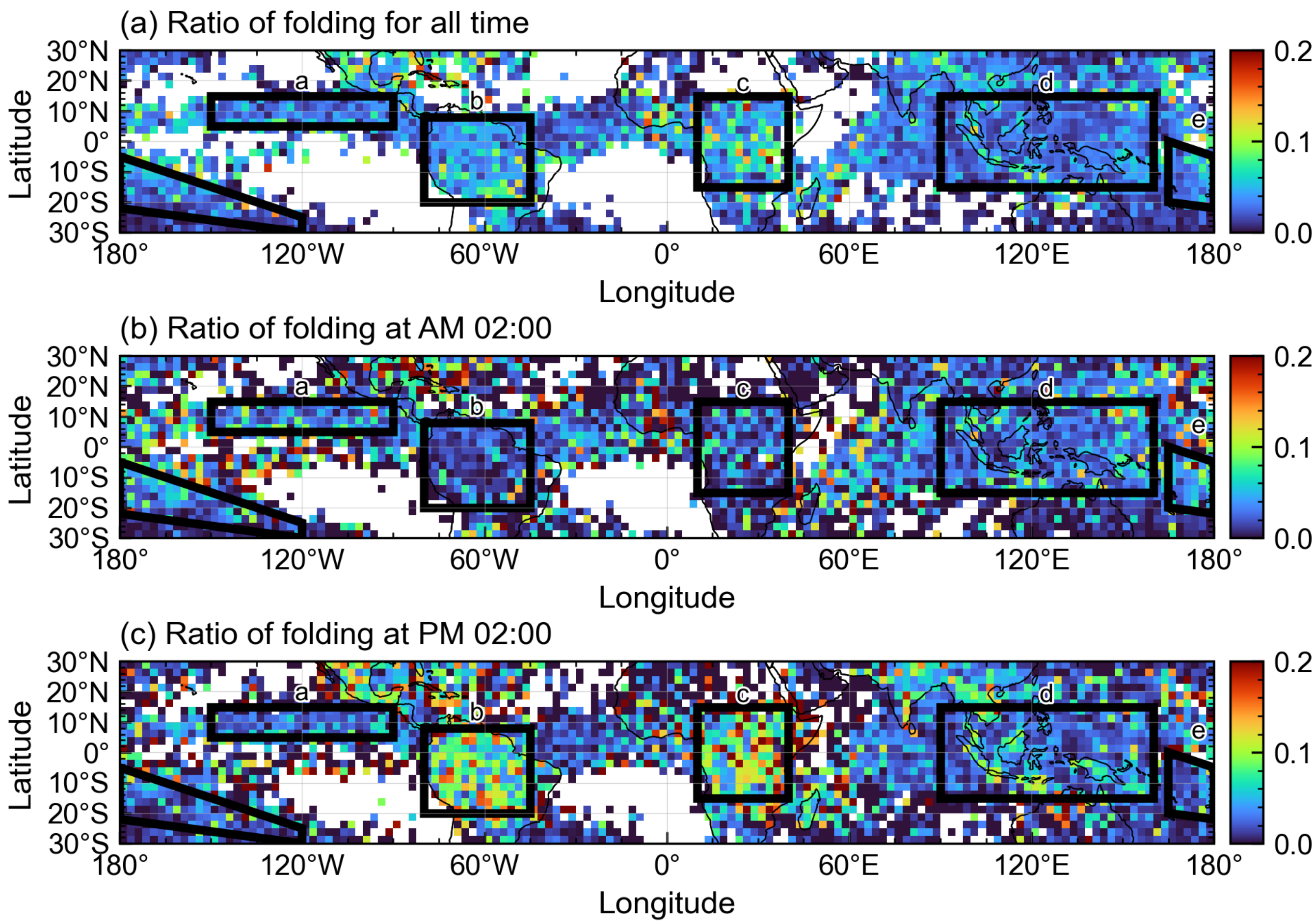

Figure 11: Spatial distribution of Doppler-velocity folding (aliasing) occurrence over the tropics (30°S–30°N). Colors indicate, for each 2.5° × 2.5° grid box, the fraction of selected columns in which at least one folding event is detected in the Doppler-velocity profiles (Sect. 2.3). (a) All overpasses combined. (b) Nighttime overpasses (~02:00 LT; ascending node). (c) Daytime overpasses (~14:00 LT; descending node). Grid boxes with fewer than 100 total columns are masked. Black rectangles labeled a–e indicate the regions used for the regional analyses (EPAC–ITCZ, Amazon, central Africa, Maritime Continent, and SPCZ).

Table 3: Regional folding occurrence. Regional and local-time statistics of Doppler-velocity folding (aliasing). For each domain and local overpass time (All, ≈02:00 LT, and ≈14:00 LT), the table lists the total number of selected columns, the number of columns in which at least one folding event is detected in the Doppler-velocity profiles (Sect. 2.3), and the resulting folding fraction (%), defined as (folded columns / total columns) × 100. Region definitions follow Fig. 11 (see Sect. 2.2).

	orbit	ALL	Central Africa	Amazon	Maritime Continent	EPAC-ITCZ	SPCZ
Total Count	All	1394477	76292	115889	340435	63878	92246

https://doi.org/10.5194/egusphere-2026-659
Preprint. Discussion started: 5 February 2026

	02:00 LT	724377	46276	67803	175238	31052	46973
	14:00 LT	670100	30016	48086	165197	32826	45273
	All	45317	3706	4821	9730	1918	2761
	02:00 LT	20896	1076	1287	5035	1088	1637
Folding count	14:00 LT	24421	2630	3534	4695	830	1124
	All	3.2%	4.9%	4.2%	2.9%	3.0%	3.0%
	02:00 LT	2.9%	2.3%	1.9%	2.9%	3.5%	3.5%
Folding ratio	14:00 LT	3.6%	8.8%	7.3%	2.8%	2.5%	2.5%

4 Summary and Discussion

This study exploits the first global, spaceborne Doppler velocity observations from the EarthCARE/CPR to diagnose updraft strength in tropical convective clouds and to relate it to the vertical structure of W-band (94 GHz) radar reflectivity. Whereas most previous satellite studies have inferred convective intensity using indirect proxies, we directly analyze vertical particle motions. Importantly, we examine not only mature deep convective systems but also lower-topped convective clouds, which are often underrepresented in legacy intensity metrics.

We analyzed EarthCARE/CPR observations from January to September 2025 over the tropical region (30° S–30° N) and applied a Doppler velocity (Vd) quality-control procedure that masks weak echoes, restricts quantitative diagnostics to range gates colder than 273.15 K, applies modest spatial averaging, and flags residual velocity folding. We define *MaxVd* as the maximum upward (positive) Doppler velocity within the subfreezing portion of each profile and classify strong-updraft columns (SU) as those with *MaxVd* > 2.5 m s^{-1}.

These SU columns account for approximately 6.7% of all nonfolded columns, indicating that they are relatively rare yet dynamically important. Examining SU occurrence as a function of cloud-top height (CTH), the 0 dBZ echo-top height [ETH(0)], and the 10 dBZ echo-top height [ETH(10)], we find that SU columns exhibit systematically higher CTH and, more notably, higher ETH(0) and ETH(10). Mapping the SU fraction onto the two-dimensional space spanned by CTH and ETH(0) further shows that SU occurrence is concentrated where ΔH ≡ CTH − ETH(0) is small. This small ΔH suggests that large hydrometeors are lofted to near the cloud top. Although large ETH and small ΔH have traditionally been used as indirect proxies for convective intensity (Luo et al., 2008; Luo et al., 2011; Takahashi and Luo, 2014), this study demonstrates the

https://doi.org/10.5194/egusphere-2026-659
Preprint. Discussion started: 5 February 2026

validity of these proxies through direct measurements of Vd and further identifies which proxy is most closely associated with Vd.

Figure 12 summarizes the relationship between updraft strength and the vertical structure of radar reflectivity. When the 0 and 10 dBZ echo-top heights rise close to the cloud top, the separations CTH–ETH(0) and CTH–ETH(10) become small, and columns tend to host strong updrafts even when the cloud-top height itself is modest (Fig. 11a,b). In contrast, when reflectivity increases gradually downward from the cloud top and both the 0 and 10 dBZ levels remain well below the CTH, updrafts are typically weak (Fig. 11c). These results indicate that the reflectivity structure beneath the cloud top can serve as a robust proxy for updraft strength: smaller CTH–ETH(0) separations correspond to stronger updrafts, whereas larger separations correspond to weaker updrafts.

This finding provides direct observational support for CloudSat-era intensity proxies based on small CTH–ETH(0) separations (e.g., Takahashi and Luo, 2014; Takahashi et al., 2017, 2023; Liu et al., 2007). The novelty of this study lies in leveraging direct Doppler velocity measurements to move beyond the proxy-based estimates of convective intensity used in previous satellite studies. Our results support the central premise of proxy approaches but also refine it by ranking the tested indicators: the cloud-top–echo-top separation ΔH ($CTH - ETH(0)$) is the most informative metric for identifying strong updrafts, followed by ETH(10), ETH(0), and finally CTH. This interpretation is consistent with the physical picture described by Takahashi et al. (2023), in which strong updrafts in developing convective cores are accompanied by a rapid upward extension of the radar echo top.

Regionally, SU columns occur more frequently over continental areas such as central Africa and the Amazon Basin and less frequently over oceanic convergence zones (e.g., the eastern Pacific ITCZ and the SPCZ) and mixed land–sea regions such as the Maritime Continent. When comparing the 02:00 and 14:00 LT overpasses, oceanic regions exhibit either a slight nighttime enhancement of SU or little diurnal contrast, whereas continental regions tend to show significantly higher SU occurrence at 14:00 LT. Structurally, during the afternoon over Africa and the Amazon, CTH and ETH(0) are not exceptionally large in absolute terms; instead, the separation $\Delta H = CTH - ETH(0)$ remains consistently small. Moreover, across most (CTH, ETH(0)) combinations, the local SU fraction in these continental hotspots substantially exceeds the tropical-mean value, indicating that the environment favors stronger updrafts even for clouds with comparable vertical development. We interpret this enhancement as reflecting a greater contribution from developing-to-mature convective cores characterized by small ΔH, rather than from unusually tall clouds, thereby explaining the elevated SU occurrence.

Taken together, these results reinforce the interpretation in Fig. 12 that ΔH is a key structural discriminator of strong updrafts. Regional and diurnal variations in SU occurrence are governed not by how high clouds grow but by how closely the radar echo top approaches the cloud top. Continental afternoon environments, characterized by a high frequency of horizontally compact convective columns with small ΔH, are particularly conducive to strong Doppler-derived updrafts, whereas regimes dominated by horizontally extensive, stratiform-rich systems tend to exhibit lower SU fractions even when cloud tops are high. This establishes a physically consistent link between regional contrasts in Doppler-derived updrafts and the vertical reflectivity structure of tropical convective systems.

https://doi.org/10.5194/egusphere-2026-659
Preprint. Discussion started: 5 February 2026

Even after quality control, velocity folding is detected in approximately 3.3% of columns. The folding frequency increases with increasing CTH and ETH(0) and is especially high where ΔH is small. Folding occurs most frequently over continental early-afternoon hotspots of intense convection, such as central Africa and the Amazon Basin. In both their vertical radar-reflectivity structure and their spatiotemporal characteristics, columns affected by folding closely resemble those with high SU fractions. Although folding cannot be used as a quantitative metric of updraft strength, its occurrence serves as a useful qualitative tracer of extreme updrafts. Because the analyses in Sects. 3.1 and 3.2 are restricted to unfolded columns, it is likely that the most intense convective cases are not fully represented in these analyses.

These measurements help close a long-standing observational gap in global constraints on convective updrafts and enable the development of a new dynamical climatology. This climatology can be used to calibrate convective parameterizations in global climate models (GCMs) and to benchmark explicitly resolved convection in global kilometer-scale simulations. A key question for numerical models is whether they reproduce (i) regional and diurnal contrasts in the frequency of strong updrafts and (ii) the joint statistics of updraft intensity and radar-echo structure documented here. Takahashi et al. (2025) compared deep convective clouds simulated by global storm-resolving models with CloudSat observations over three tropical "chimney" regions: tropical Africa, tropical Amazonia, and the tropical warm pool. Within that framework, cloud-top height and radar-derived echo-top metrics could be evaluated against CloudSat observations; however, updraft intensity could not be validated because CloudSat lacks Doppler velocity measurements. Consequently, comparisons of updraft strength were necessarily limited to inter-model differences and proxy-based diagnostics. These studies identified substantial biases in convective intensity and precipitation formation: updraft indicators in the tropical warm pool are often too strong, while precipitation forms at unrealistically high altitudes under weak vertical velocities, indicating inconsistencies between cloud dynamics and microphysics. Our EarthCARE-based diagnostics overcome this limitation by directly linking *MaxVd* to the vertical structure of radar reflectivity and by quantifying regional and diurnal variations in the occurrence of strong updrafts (SU). These constraints enable rigorous tests of whether models not only reproduce observed cloud-top and precipitation-top heights but also associate these structures with realistic updraft velocities, thereby providing a process-oriented pathway to improve the coupling between convective dynamics and microphysics in both parameterized and explicitly resolved convection.

Despite these advances, this study has several limitations that highlight priorities for future work. First, our analysis is based on a nine-month record, which is too short to characterize the full range of intraseasonal and interannual variability, including the Madden–Julian Oscillation (MJO) and the El Niño–Southern Oscillation (ENSO). Extending the analysis to multi-year data sets will be essential for quantifying how long-period variability modulates convective updrafts. Second, to ensure data quality in the quantitative analyses in Sects. 3.1 and 3.2, we excluded columns affected by Doppler velocity folding. Because folding preferentially occurs in the strongest updrafts, our statistics likely underestimate both the frequency and magnitude of the most extreme convective events. This under-sampling may also reduce the apparent land–ocean contrast relative to climatologies based on precipitation-radar echo-top heights from GPM (Houze et al., 2015; Liu and Zipser, 2015) and lightning-based proxies (Albrecht et al., 2016). Developing a physically based unfolding algorithm for the CPR is therefore a high priority to mitigate this bias. Third, we restricted the diagnosis to subfreezing regions (temperature < 273.15 K) to avoid

https://doi.org/10.5194/egusphere-2026-659
Preprint. Discussion started: 5 February 2026

Doppler velocity aliasing from large-particle sedimentation. This restriction excludes cloud systems with cloud-top temperatures above 273.15 K from the analysis and limits the assessment of updrafts to the upper levels of the targeted clouds. Fourth, because the CPR operates at W band, it is susceptible to strong attenuation in heavy precipitation, which can obscure reflectivity at lower altitudes, as suggested by SU columns (Fig. 5). As a result, we cannot yet directly evaluate echo-top-height climatologies at 20–40 dBZ derived from the TRMM and GPM precipitation radars.

Future work should integrate this unique Doppler-velocity dataset with complementary observing systems. Combining EarthCARE Doppler-velocity measurements with GPM precipitation estimates (Aoki et al., 2026), lightning observations, and cloud life-cycle metrics from geostationary satellites would enable a more holistic characterization of deep convection. Such an integrated framework would allow for the systematic evaluation and recalibration of legacy intensity proxies and support the development of a comprehensive intensity index that integrates ETH, ΔH, electrification, and life-cycle phase.

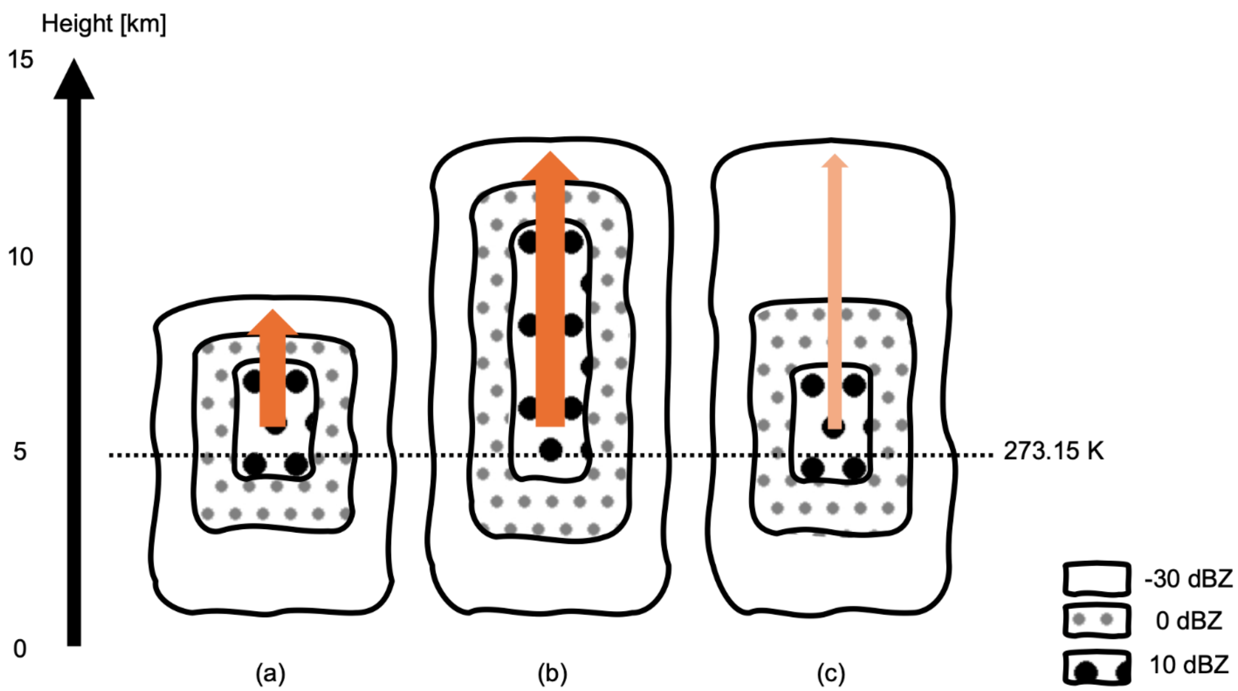

Figure 12: Conceptual schematic of typical radar-reflectivity structures associated with strong and weak updraft columns. Grey, dotted, and filled-dot outlines indicate the regions exceeding −30, 0, and 10 dBZ, respectively. Orange arrows illustrate updraft strength qualitatively. Panels (a–b) show strong-updraft cases in which the 0 and 10 dBZ echo tops rise close to the cloud top (small CTH–ETH(0)), including a moderately deep cloud (a). Panel (c) shows a weak-updraft case characterized by a top-light structure in which reflectivity increases gradually downward and both ETH(0) and ETH(10) remain well below the cloud top.

Data availability

The EarthCARE/CPR L2A CPR one-sensor Cloud Products (https://doi.org/10.57746/EO.01jdvd2gqq34e6yz9p8kfe68x5, JAXA, 2025a) used in this study can be downloaded from the JAXA G-Portal (https://gportal.jaxa.jp/gpr/).

Author contributions

HH conceptualized the study, performed the formal analysis, developed the methodology, and prepared the visualizations. KS contributed to the conceptualization and acquired the funding. MK and SA conducted the investigation and provided feedback on the results. TK conducted the investigation and supervised the study. HH wrote the original draft of the manuscript. KS, MK, SA, and TK contributed to the review and editing of the manuscript.

Competing interests

The contact author has declared that none of the authors has any competing interests.

Special issue statement

This article is part of the special issue “Early results from EarthCARE (AMT/ACP/GMD inter-journal SI)”. It is not associated with a conference.

Acknowledgements

ChatGPT was used to assist the editing the language of parts of the manuscript. All content was subsequently reviewed and edited by the authors, who take full responsibility for the final version of the manuscript. We would also like to thank Editage (www.editage.jp) for English language editing.

Financial support

This study was supported by JAXA/EarthCARE project, MEXT program for the Advanced Studies of Climate Change Projection (SENTAN) (Grant JPMXD0722680395), and JST Moonshot R&D (Grant JPMJMS2281).

References

Abbott, T. H., Jeevanjee, N., Cheng, K.-Y., Zhou, L., and Harris, L.: The land-ocean contrast in deep convective intensity in a global storm-resolving model, J. Adv. Model. Earth Syst., 17, 5, https://doi.org/10.1029/2024MS004467, 2025.

https://doi.org/10.5194/egusphere-2026-659
Preprint. Discussion started: 5 February 2026

Adler, R. F. and Fenn, D. D.: Thunderstorm vertical velocities estimated from satellite data, Mon. Weather Rev., 107, 1747–1754, https://doi.org/10.1175/1520-0469(1979)036<1747:TVVEFS>2.0.CO;2, 1979.

Albrecht, R. I., Goodman, S. J., Buechler, D. E., Blakeslee, R. J., and Christian, H. J.: Where Are the Lightning Hotspots on Earth?, B. Am. Meteorol. Soc., 97, 2051–2068, https://doi.org/10.1175/BAMS-D-14-00193.1, 2016.

Aoki, S., Kubota, T., and Turk, F. J.: Exploring vertical motions in convective and stratiform precipitation using spaceborne radar observations: Insights from EarthCARE and GPM coincidence dataset, Atmos. Meas. Tech., 19, 79–100, https://doi.org/10.5194/amt-19-79-2026, 2026.

Battaglia, A., Augustynek, T., Tanelli, S., and Kollias, P.: Multiple scattering identification in spaceborne W-band radar measurements of deep convective cores, J. Geophys. Res.-Atmos., 116, D19, https://doi.org/10.1029/2011JD016142, 2011.

Battaglia, A.: Impact of second-trip echoes for space-borne high-pulse-repetition-frequency nadir-looking W-band cloud radars, Atmos. Meas. Tech., 14, 7809–7820, https://doi.org/10.5194/amt-14-7809-2021, 2021.

Bechtold, P., Bazile, E., Guichard, F., Mascart, P., and Richard, E.: A mass-flux convection scheme for regional and global models, Q. J. R. Meteorol. Soc., 127, 869–886, https://doi.org/10.1002/qj.49712757309, 2001.

Bedka, K., Brunner, J., Dworak, R., Feltz, W., Otkin, J., and Greenwald, T.: Objective satellite-based detection of overshooting tops using infrared window channel brightness temperature gradients, J. Appl. Meteor. Climatol., 49, 181–202, https://doi.org/10.1175/2009JAMC2286.1, 2010.

Cecil, D. J., Goodman, S. J., Boccippio, D. J., Zipser, E. J., and Nesbitt, S. W.: Three years of TRMM precipitation features. Part I: Radar, radiometric, and lightning characteristics, Mon. Weather Rev., 133, 543–566, https://doi.org/10.1175/MWR-2876.1, 2005.

Christian, H. J., Blakeslee, R. J., Boccippio, D. J., Boeck, W. L., Buechler, D. E., Driscoll, K. T., Goodman, S. J., Hall, J. M., Koshak, J. M., Mach, D. M., and Stewart, M. F.: Global frequency and distribution of lightning as observed from space by the Optical Transient Detector, J. Geophys. Res. Atmos., 108, ACL 4-1-ACL 4-15, https://doi.org/10.1029/2002JD002347, 2003.

Christopoulos, C. and Schneider, T.: Assessing biases and climate implications of the diurnal precipitation cycle in climate models, Geophys. Res. Lett., 48, e2021GL093017, https://doi.org/10.1029/2021GL093017, 2021.

Collis, S., Protat, A., May, P. T., and Williams, C.: Statistics of storm updraft velocities from TWP-ICE including verification with profiling measurements, J. Appl. Meteor. Climatol., 52, 1909–1922, https://doi.org/10.1175/JAMC-D-12-0230.1, 2013.

Deierling, W. and Petersen, W. A.: Total lightning activity as an indicator of updraft characteristics, J. Geophys. Res. Atmos., 113, D16, https://doi.org/10.1029/2007JD009598, 2008.

Doviak, R. J. and Zrnić, D. S.: Doppler Radar & Weather Observations: Second Edition, Academic Press, ISBN 148329482X, 9781483294827, 2014.

Eisinger, M., Marnas, F., Wallace, K., Kubota, T., Tomiyama, N., Ohno, Y., Tanaka, T., Tomita, E., Wehr, T., and Bernaerts, D.: The EarthCARE mission: science data processing chain overview, Atmos. Meas. Tech., 17, 839–862, https://doi.org/10.5194/amt-17-839-2024, 2024.

Galfione, A., Battaglia, A., Puigdomènech Treserras, B., and Kollias, P.: First insights into deep convection by the Doppler velocity measurements of the EarthCARE Cloud Profiling Radar, Atmos. Meas. Tech., 18, 6747–6763, https://doi.org/10.5194/amt-18-6747-2025, 2025.

Giangrande, S. E., Toto, T., Jensen, M. P., Bartholomew, M. J., Feng, Z., Protat, A., Williams, C. R., Schumacher, C., and Machado, L.: Convective cloud vertical velocity and mass-flux characteristics from radar wind profiler observations during GoAmazon2014/5, J. Geophys. Res.-Atmos., 121, 12891–12913, https://doi.org/10.1002/2016JD025303, 2016.

Houze, R. A., Jr., Rasmussen, K. L., Zuluaga, M. D., and Brodzik, S. R.: The variable nature of convection in the tropics and subtropics: A legacy of 16 years of the Tropical Rainfall Measuring Mission (TRMM) satellite, Rev. Geophys., 53, 994–1029, https://doi.org/10.1002/2015RG000488, 2015.

Hagihara, Y., Ohno, Y., Horie, H., Roh, W., Satoh, M., and Kubota, T.: Global evaluation of Doppler velocity errors of EarthCARE cloud-profiling radar using a global storm-resolving simulation., Atmos. Meas. Tech., 16, 3211–3219, https://doi.org/10.5194/amt-16-3211-2023, 2023.

Hamada, A., Takayabu, Y. N., C. Liu, and E. J. Zipser: Weak linkage between the heaviest rainfall and tallest storms, Nat. Commun., 6, 6213, https://doi.org/10.1038/ncomms7213, 2015.

Hamada, A. and Takayabu, Y. N.: Convective cloud top vertical velocity estimated from geostationary satellite rapid-scan measurements, Geophys. Res. Lett., 43, 5435–5441, https://doi.org/10.1002/2016GL068962, 2016.

Hartmann, D. L., Moy, L. A., and Fu, Q.: Tropical convection and the energy balance at the top of the atmosphere, J. Climate, 14, 4495–4511, https://doi.org/10.1175/1520-0442(2001)014<4495:TCATEB>2.0.CO;2, 2001.

Heymsfield, G. M., Tian, L., Heymsfield, A. J., Li, L., and Guimond, S.: Characteristics of deep tropical and subtropical convection from nadir-viewing high-altitude airborne Doppler radar, J. Atmos. Sci., 67, 285–308, https://doi.org/10.1175/2009JAS3132.1, 2010.

Hou, A. Y., Kakar, R. K., Neeck, S., Azarbarzin, A. A., Kummerow, C. D., Kojima, M., Oki, R., Nakamura, K., and Iguchi, T.: The Global Precipitation Measurement mission, Bull. Amer. Meteor. Soc., 95, 701–722, https://doi.org/10.1175/BAMS-D-13-00164.1, 2014.

Iguchi, T., Kozu, T., Meneghini, R., Awaka, J., and Okamoto, K.: Rain-profiling algorithm for the TRMM precipitation radar, J. Appl. Meteor.., 39, 2038-2052, https://doi.org/10.1175/1520-0450(2001)040<2038:RPAFTT>2.0.CO;2, 2000.

Illingworth, A. J., Barker, H. W., Beljaars, A., Ceccaldi, M., Chepfer, H., Clerbaux, N., Cole, J., Delanoë, J., Domenech, C., Donovan, D. P., Fukuda, S., Hirakata, M., Hogan, R. J., Huenerbein, A., Kollias, P., Kubota, T., Nakajima, T., Nakajima, T. Y., Nishizawa, T., Ohno, Y., Okamoto, H., Oki, R., Sato, K., Satoh, M., Shephard, M., Velázquez-Blázquez, A., Wandinger, U.,Wehr, T., and van Zadelhoff, G.-J.: The EarthCARE Satellite: The next step forward in global measurements of clouds, aerosols, precipitation and radiation, B. Am. Meteorol. Soc., 96, 1311–1332, https://doi.org/10.1175/BAMS-D-12-00227.1, 2015.

JAXA, EarthCARE/CPR L2A CPR one-sensor Cloud Products. https://doi.org/10.57746/EO.01jdvd2gqq34e6yz9p8kfe68x5, last access: 5 January 2026, 2025a.

https://doi.org/10.5194/egusphere-2026-659
Preprint. Discussion started: 5 February 2026

JAXA, EarthCARE JAXA Level 2 Algorithm Theoretical Basis Document (L2 ATBD), https://www.eorc.jaxa.jp/EARTHCARE/document/JAXAL2ProductList/ATBD/NDX-110018N_EarthCARE_L2_ATBD_draft_rev2.pdf, last access: 5 January 2026, 2025b.

JAXA, Release notes for the EarthCARE/CPR Level-1b Product, available from https://www.eorc.jaxa.jp/EARTHCARE/document/L1ProductList/ReleaseNote/CPR/SEC-2024057-0D_Release_Notes_for_EarthCARE_CPR_L1b_Product.pdf, last access: 5 January 2026, 2025c.

Kikuchi, M. and Suzuki, K.: Characterizing vertical particle structure of precipitating cloud system from multiplatform measurements of A‐Train constellation. Geophys. Res. Lett., 46, 1040-1048, https://doi.org/10.1029/2018GL081244, 2019.

Kollias, P., Tanelli, S., Battaglia, A., and Tatarevic, A.: Evaluation of EarthCARE cloud profiling radar Doppler velocity measurements in particle sedimentation regimes, J. Atmos. Oceanic Technol., 31, 366–386, https://doi.org/10.1175/JTECH-D-11-00202.1, 2014.

Kollias, P., Battaglia, A., Lamer, K., Treserras, B. P., and Braun, S. A.: Mind the gap-part 3: Doppler velocity measurements from space, Front. Remote Sens., 3, 860 84, https://doi.org/10.3389/frsen.2022.860284, 2022.

Koren, I., Altaratz, O., Feingold, G., Levin, Z., and Reisin, T.: Cloud's Center of Gravity – a compact approach to analyze convective cloud development, Atmos. Chem. Phys., 9, 155–161, https://doi.org/10.5194/acp-9-155-2009, 2009.

Kummerow, C., Barnes, W., Kozu, T., Shiue, J., and Simpson, J.: The Tropical Rainfall Measuring Mission (TRMM) sensor package, J. Atmos. Oceanic Technol., 15, 809–817, https://doi.org/10.1175/1520-0426(1998)015<0809:TTRMMT>2.0.CO;2, 1998.

LeMone, M. A., and E. J. Zipser: Cumulonimbus vertical velocity events in GATE. Part I: Diameter, intensity and mass flux, J. Atmos. Sci., 37, 2444–2457, https://doi.org/10.1175/1520-0469(1980)037<2444:CVVEIG>2.0.CO;2, 1980.

Li, Y., Liu, Y., Chen, Y., Chen, B., Zhang, X., Wang, W., Shu, Z., and Huo, Z.: Characteristics of Deep Convective Systems and Initiation during Warm Seasons over China and Its Vicinity, Remote Sensing, 13, 4289, https://doi.org/10.3390/rs13214289, 2021.

Liu, C. and Zipser, E. J.: Global distribution of convection penetrating the tropical tropopause, J. Geophys. Res. Atmos., 110, D23104, https://doi.org/10.1029/2005JD006063, 2005.

Liu, C., Zipser, E. J., and Nesbitt, S. W.: Global distribution of tropical deep convection: different perspectives from TRMM infrared and radar data, J. Climate, 20, 489-503, https://doi.org/10.1175/JCLI4023.1, 2007.

Liu, C., E. J. Zipser, D. J. Cecil, S. W. Nesbitt, and S. Sherwood: A cloud and precipitation feature database from nine years of TRMM observations, J. Appl. Meteorol. Climatol., 47, 2712–2728, https://doi.org/10.1175/2008JAMC1890.1, 2008.

Liu, C. and Zipser, E. J.: The global distribution of largest, deepest, and most intense precipitation systems, Geophys. Res. Lett., 42, 3591–3596, https://doi.org/10.1002/2015GL063776, 2015.

Lucas, C., Zipser, E. J., and LeMone, M. A.: Vertical velocity in oceanic convection off tropical Australia in early morning: Roles of buoyancy and dynamic pressure, J. Atmos. Sci., 51, 3183–3193, https://doi.org/10.1175/1520-0469(1994)051<3183:VVIOCO>2.0.CO;2, 1994.

https://doi.org/10.5194/egusphere-2026-659
Preprint. Discussion started: 5 February 2026

Luo, Y., Zhang, R., and Wang, H.: Comparing occurrences and vertical structures of hydrometeors between eastern China and the Indian monsoon region using CloudSat/CALIPSO data. J. Climate, 22, 1052-1064, https://doi.org/10.1175/2008JCLI2606.1, 2009.

Luo, Y., Zhang, R., Qian, W., Luo, Z., and Hu, J.: Intercomparison of deep convection over the Tibetan Plateau–Asian monsoon region and subtropical North America in boreal summer using CloudSat/CALIPSO data, J. Climate, 24, 2164–2177, https://doi.org/10.1175/2010JCLI4032.1, 2011.

Luo, Z. J., Liu, C., and Stephens, G. L.: CloudSat adding new insight into tropical penetrating convection, Geophys. Res. Lett., 35, 19, https://doi.org/10.1029/2008GL035330, 2008.

Luo, Z. J., Jeyaratnam, J., Iwasaki, S., Takahashi, H., and Anderson, R.: Convective vertical velocity and cloud internal vertical structure: An A-Train perspective, Geophys. Res. Lett., 41, 723-729, https://doi.org/10.1002/2013GL058922, 2014.Masunaga, H. and Kummerow, C. D.: Observations of tropical precipitating clouds ranging from shallow to deep convective systems, Geophys. Res. Lett., 33, L16805, https://doi.org/10.1029/2006GL026547, 2006.Maloney, E. D., Gettelman, A., Ming, Y., Neelin, J. D., Barrie, D., Mariotti, A., Chen, C.-C., Coleman, D. R. B., Kuo, Y.-H., Singh, B., Annamalai, H., Berg, A., Booth, J. F., Camargo, S. J., Dai, A., Gonzalez, A., Hafner, J., Jiang, X., Jing, X., Kim, D., Kumar, A., Moon, Y., Naud, C. M., Sobel, A. H., Suzuki, K., Wang, F., Wang, J., Wing, A. A., Xu, X., and Zhao, M.: Process-Oriented Evaluation of Climate and Weather Forecasting Models, B. Am. Meteorol. Soc., 100, 1665–1686, https://doi.org/10.1175/bams-d-18-0042.1, 2019.

Manabe, S., Smagorinsky, J., and Strickler, R. F.: Simulated climatology of a general circulation model with a hydrologic cycle, Mon. Weather Rev., 93, 769–798, https://doi.org/10.1175/1520-0493(1965)093<0769:SCOAGC>2.3.CO;2, 1965.

Masunaga, H., L'Ecuyer, T. S., and Kummerow, C. D.: Variability in the characteristics of precipitation systems in the tropical Pacific. Part I: Spatial structure. J. Climate, 18, 823-840., https://doi.org/10.1175/JCLI-3304.1, 2005.

Matrosov, S. Y.: Potential for attenuation-based estimations of rainfall rate from CloudSat, Geophys. Res. Lett., 34, 5, https://doi.org/10.1029/2006GL029161, 2007

Mohr, K. I. and Zipser, E. J.: Defining mesoscale convective systems by their 85-GHz ice scattering signatures, B. Am. Meteorol. Soc., 77, 1179–1190, https://doi.org/10.1175/1520-0477(1996)077<1179:DMCSBT>2.0.CO;2, 1996.

Nesbitt, S. W., and Zipser, E. J.: The diurnal cycle of rainfall and convective intensity according to three years of TRMM measurements. J. Climate, 16, 1456-1475, https://doi.org/10.1175/1520-0442(2003)016<1456:TDCORA>2.0.CO;2, 2003

Pilewskie, J. A. and L'Ecuyer, T. S.: The Global Nature of Early-Afternoon and Late-Night Convection Through the Eyes of the A-Train, J. Geophys. Res.-Atmos., 127, e2022JD036438, https://doi.org/10.1029/2022JD036438, 2022.

Price, C. and Rind, D.: A simple lightning parameterization for calculating global lightning distributions, J. Geophys. Res.-Atmos., 97, 9919–9933, https://doi.org/10.1029/92JD00719, 1992.

Ramanathan, V. L., Cess, R. D., Harrison, E. F., Minnis, P., Barkstrom, B. R., Ahmad, E., and Hartmann, D.: Cloud-radiative forcing and climate: Results from the Earth Radiation Budget Experiment, Science, 243, 57-63, https://doi.org/10.1126/science.243.4887.57, 1989.

Romatschke, U., Medina, S., and Houze, R. A., Jr.: Regional, seasonal, and diurnal variations of extreme convection in the South Asian region, J. Climate, 23, 419–439, https://doi.org/10.1175/2009JCLI3140.1, 2010.

Sato, K., Okamoto, H., Nishizawa, T., Jin, Y., Nakajima, T. Y., Wang, M., Satoh, M., Roh, W., Ishimoto, H., and Kudo, R.: JAXA Level 2 cloud and precipitation microphysics retrievals based on EarthCARE radar, lidar, and imager: the CPR_CLP, AC_CLP, and ACM_CLP products, Atmos. Meas. Tech., 18, 1325–1338, https://doi.org/10.5194/amt-18-1325-2025, 2025.

Schiro, K. A. and Neelin, J. D.: Tropical continental downdraft characteristics: mesoscale systems versus unorganized convection, Atmos. Chem. Phys., 18, 1997–2010, https://doi.org/10.5194/acp-18-1997-2018, 2018.

Schumacher, C., Stevenson, S. N., and Williams, C. R.: Vertical motions of the tropical convective cloud spectrum over Darwin, Australia., Q. J. Roy. Meteorol. Soc., 141, 2277–2288, https://doi.org/10.1002/qj.2520, 2015

Sherwood, S. C., Bony, S., and Dufresne, J.-L.: Spread in model climate sensitivity traced to atmospheric convective mixing, Nature, 505, 37–42, https://doi.org/10.1038/nature12829, 2014.

Skofronick-Jackson, G., Petersen, W., Berg, W., Kidd, C., Stocker, E., Kirschbaum, D., Kakar, R., Braun, S., Huffman, G., Iguchi, T., Kirstetter, P., Kummerow, C., Meneghini, R., Oki, R., Olson, W., Takayabu, Y., Furukawa, K., and Wilheit, T.: The Global Precipitation Measurement (GPM) mission for science and society, B. Am. Meteorol. Soc., 98, 1679–1695, https://doi.org/10.1175/BAMS-D-15-00306.1, 2017.

Song, H.J., Kim, S., Roh, S. and Lee, H: Difference between cloud top height and storm height for heavy rainfall using TRMM measurements, J. Meteorol. Soc. Jpn., 98, 901-914, https://doi.org/10.2151/jmsj.2020-044, 2020.

Stephens, G. L., Vane, D. G., Boain, R. J., Mace, G. G., Sassen, K., Wang, Z., Illingworth, A. J., O'Connor, E. J., Rossow, W. B., Durden, S. L., Miller, S. D., Austin, R. T., Benedetti, A., Mitrescu, C., and the CloudSat Science Team: The cloudsat mission and the A-train, Bull. Amer. Met. Soc., 83, 1771–1790, https://doi.org/10.1175/BAMS-83-12-1771, 2002.

Stephens, G., Vane, D. G., Tanelli, S., Im, E., Durden, S., Rokey, M., Reinke, D., Partain, P., Mace, G. G., Austin, R., L'Ecuyer, T., Haynes, J., Lebsock, M., Suzuki, K., Waliser, D., Wu, D., Kay, J., Gettelman, A., Wang, Z., and Marc hand, R. : CloudSat mission: Performance and early science after the first year of operation, J. Geophys. Res.-Atmos., 113, D8, https://doi.org/10.1029/2008JD009982, 2008.

Sy, O. O., Tanelli, S., Takahashi, N., Ohno, Y., Horie, H., and Kollias, P.: Simulation of EarthCARE spaceborne Doppler radar products using ground-based and airborne data: Effects of aliasing and nonuniform beam-filling, IEEE Trans. Geosci. Remote Sens., 52, 1463–1479, https://doi.org/10.1109/TGRS.2013.2251639, 2014.

Takahashi, H. and Luo, Z. J.: Characterizing tropical overshooting deep convection from joint analysis of CloudSat and geostationary satellite observations, J. Geophys. Res.-Atmos., 119, 112–121, https://doi.org/10.1002/2013JD020972, 2014.

Takahashi, H., Luo, Z. J., and Stephens, G. L.: Level of neutral buoyancy, deep convective outflow, and convective core: New perspectives based on 5 years of CloudSat data, J. Geophys. Res. Atmos., 122, 2958–2969, https://doi.org/10.1002/2016JD025969, 2017.

https://doi.org/10.5194/egusphere-2026-659
Preprint. Discussion started: 5 February 2026

Takahashi, H., Luo, Z. J., Stephens, G., and Mulholland, J. P.: Revisiting the Land-Ocean Contrasts in Deep Convective Cloud Intensity Using Global Satellite Observations, Geophysical Research Letters, 50, e2022GL102089, https://doi.org/10.1029/2022GL102089, 2023.

Takahashi, H., Wu, L., Smalley, M. A., Stephens, G., Suzuki, K., and Posselt, D. J., Land‐Ocean Differences in Tropical Deep Convective Clouds: Intercomparison of DYAMOND Simulations and CloudSat Observations, J. Geophys. Res.-Atmos., 130, 23, https://doi.org/10.1029/2025JD044688, 2025.

Tanelli, S., Im, E., Mascelloni, S. R., and Facheris, L.: Spaceborne Doppler radar measurements of rainfall: correction of errors induced by pointing uncertainties, J. Atmos. Oceanic Technol., 22, 1676–1690, https://doi.org/10.1175/JTECH1797.1, 2005.

Tanelli, S., Durden, S. L., Im, E., Pak, K. S., Reinke, D. G., Partain, P., Haynes, J. M., and Marchand, R. T.: CloudSat's Cloud Profiling Radar After Two Years in Orbit: Performance, Calibration, and Processing, IEEE T. Geosci. Remote, 46, 3560–3573, doi:10.1109/TGRS.2008.2002030, 2008.

Tian, B. and Dong, X.: The Double-ITCZ Bias in CMIP3, CMIP5, and CMIP6 Models Based on Annual Mean Precipitation, Geophys. Res. Lett., 47, e2020GL087232, https://doi.org/10.1029/2020GL087232, 2020.

Tiedtke, M.: A comprehensive mass flux scheme for cumulus parameterization in large-scale models, Mon. Weather Rev., 117, 1779–1800, https://doi.org/10.1175/1520-0493(1989)117<1779:ACMFSF>2.0.CO;2, 1989.

Wehr, T., Kubota, T., Tzeremes, G., Wallace, K., Nakatsuka, H., Ohno, Y., Koopman, R., Rusli, S., Kikuchi, M., Eisinger, M., Tanaka, T., Taga, M., Deghaye, P., Tomita, E., and Bernaerts, D.: The EarthCARE mission – science and system overview, Atmos. Meas. Tech., 16, 3581–3608, https://doi.org/10.5194/amt-16-3581-2023, 2023.

Williams, E. R. and Stanfill, S.: The physical origin of the land-ocean contrast in lightning activity, C. R. Physique, 3, 1277–1292, https://doi.org/10.1016/S0169-8095(02)00025-1, 2002.

Williams, E. R., Mushtak, V., Rosenfeld, D., Goodman, S., and Boccippio, D.: Thermodynamic conditions favorable to superlative thunderstorm updraft, mixed phase microphysics and lightning flash rate, Atmos. Res., 76, 288–306, https://doi.org/10.1016/j.atmosres.2004.11.010, 2005

Xu, W., Chen, H., Wei, H., Luo, Y., and Zhao, T.: Extreme Precipitation Produced by Relatively Weak Convective Systems in the Tropics and Subtropics, Geophys. Res. Lett., 49, e2022GL098048, https://doi.org/10.1029/2022GL098048, 2022.

Yang, G.-Y. and Slingo, J.: The diurnal cycle in the tropics, Mon. Weather Rev., 129, 784-801, https://doi.org/10.1175/1520-0493(2001)129<0784:TDCITT>2.0.CO;2, 2001.

Zhao, M.: An investigation of the connections among convection, clouds, and climate sensitivity in a global climate model, J. Climate, 27, 1845–1862, https://doi.org/10.1175/JCLI-D-13-00145.1, 2014.

Zipser, E. J., Cecil, D. J., Liu, C., Nesbitt, S. W., and Yorty, D. P.: Where are the most intense thunderstorms on Earth?, Bull. Amer. Meteor. Soc., 87, 1057–1071, https://doi.org/10.1175/BAMS-87-8-1057, 2006.